The Effect of Ocean Currents on Sea Surface Temperature Anomalies

Olwijn Leeuwenburgh

Geodetic Department, Kort & Matrikelstyrelsen

Rentemestervej 8, 2400 Copenhagen NV

Denmark

ol@kms.dk

and

Detlef Stammer [1]

Physical Oceanography Research Division

Scripps Institution of Oceanography, La Jolla

dstammer@ucsd.edu

August 8, 2000

Submitted to

Journal of Physical Oceanography

[1]Corresponding author: Detlef Stammer, Scripps Institution of Oceanography, 9500 Gilman Dr. MS 0230, La Jolla, 92393-0230; dstammer@ucsd.edu; ph: (858) 822-3376

Abstract

We investigate regional and global-scale correlations between observed anomalies in sea surface temperature and height. A strong agreement between the two fields is found over a broad range of latitudes for different ocean basins. Both time-longitude plots and wavenumber-frequency spectra suggest an advective forcing of SST anomalies by a first-mode baroclinic wave field on spatial scales down to 400 km and time scales as short as 1 month. Even though the magnitude of the mean background temperature gradient is determining for the effectiveness of the forcing, there is no obvious seasonality that can be detected in the amplitudes of SST anomalies. Instead, individual wave signatures in the SST can in some cases be followed over periods of two years.

The phase relationship between SST and SSH anomalies is dependent upon frequency and wavenumber and displays a clear decrease of the phase lag toward higher latitudes where the two fields come into phase at low frequencies. Estimates of the damping coefficient are larger than generally obtained for a purely atmospheric feedback. From a global frequency spectrum a damping time scale of 2-3 month was found. Regionally results are very variable and range from 1 month near strong currents to 10 month at low latitudes and in the sub-polar North Atlantic. Strong agreement is found between the first global EOF modes of 10 day averaged and spatially smoothed SST and SSH grids. The accompanying time series display low frequency oscillations in both fields.

1 Introduction

On the annual period, large-scale sea surface temperature (SST) is primarily controlled by local air-sea fluxes of heat (Gilll and Niller, 1973). However, details about processes governing SST anomalies on intra-seasonal, and interannual to decadal periods are less well understood (Kushnir and Held, 1996; Frankignoul, 1999). On these longer time scales a substantial fraction of the memory of the climate system must reside in the ocean, and knowing how the ocean interior communicates with the surface layers and the overlaying atmosphere is an important issue to be solved in climate research.

In most general terms, changes in SST are governed through the heat balance in the so-called surface *mixed layer* of the ocean which is strongly influenced by turbulent fluxes of momentum and buoyancy (heat and fresh water) at the sea surface, entrainment processes at its lower boundary, and by other advective and diffusive processes within the mixed layer itself. Its vertically integrated heat and salt content varies significantly from one season to the next, as does its vertical extent. Away from the tropical regions, the mixed-layer depth reaches a maximum at the end of a cooling season characterized by strong winds and low air temperatures, and reaches its minimum in summer under reversed conditions.

The general assumption is that the mixed layer is nearly decoupled from the interior ocean during the warming phase, extending through late summer. Consistent with that picture would be that the deep ocean is dynamically shielded from the atmosphere and consequently, that the interaction of anomalous sub-surface ocean structures with the atmosphere is limited primarily to winter months (Cayan, 1992; Kushnir, 1994). However, as we will demonstrate here, this concept is not entirely consistent with global altimetric sea surface height (SSH) and SST observations. Because sea surface height fields reflect vertical integrals of oceanic currents over much of the deeper water column, primarily the thermocline, the variability in SST and SSH should be uncorrelated

to a good approximation except on the annual period. Instead, striking large-scale correlations have been reported between both fields (see e.g., Nerem et al., 1999; Leuliette and Wahr, 1999) leading to serious questions regarding our understanding of processes responsible for observed SST and SSH variations, their relation to surface heat fluxes, changes in the oceanic heat content, and ocean dynamics.

To gain further insight into the role the ocean plays in setting observed SST patterns, we will therefore investigate here (1) the relation between Reynolds and Smith (1994) SST data and TOPEX/POSEIDON SSH data; (2) the relation of variations in both fields to local surface forcing and ocean dynamics; and (3) implications of those relations for our understanding of processes governing SST and SSH changes and air-sea coupling mechanisms.

We will start in Section 2 with a global comparison of large-scale SST and SSH anomalies, their EOF's and global SST frequency and wavenumber spectra. In Section 3 we will then give a discussion of SST and SSH on spatial scales smaller than about 1000km along longitude-time sections and will interpret results in terms of horizontal advection of the temperature fields by the anomalous ocean currents. In Section 4 we will then give a broader discussion of important mechanisms leading to observed SST anomalies based on scaling arguments.

2 Large-scale SSH and SST Anomalies

We will begin with a comparison of SST anomalies T' as they emerge from the Reynolds and Smith (1994) analysis, with anomalies in SSH, η', resulting from the TOPEX/POSEIDON altimeter data set. TOPEX/POSEIDON data from the period October 1992 through end of 1998 were processed in a standard manner as described by Stammer and Wunsch (1994) and King et al. (1995). Data from each individual nominal 10-day repeat cycle (in practice the repeat cycle is 9.92 days) were gridded

on a 2° by 2° spatial grid. The Reynolds and Smith (1994) SST analysis fields were obtained from NCEP on a 1° by 1° global grid. This product is based on AVHRR images of skin temperature which were combined with ship and buoy data into weekly estimates of the surface bulk temperature using an objective analysis procedure (we will refer to these temperatures as SST). We interpolated these weekly fields here onto the 10-day TOPEX/POSEIDON cycles to match the SSH time sampling.

Because our emphasis is on anomalies not associated with the averaged large-scale seasonal heating and cooling cycle, the annual and semi-annual harmonics were removed from both data sets to obtain anomalies T' and η'. The seasonal cycle in SST is very pronounced, representing 95% of its variance. It represents about 55% of the variance in SSH observations and masks most of the mid-latitude dynamical ocean signal. The seasonal cycle in SSH represents mostly a steric effect associated with a changing heat content of the surface layers above the seasonal thermocline. However, in some locations, notably the North Pacific, a seasonal cycle in SSH is also related to a mass-redistribution due to changing wind stress fields (e.g., compare Stammer, 1997), but which is not of further interest here.

2.1 Comparison of SSH and SST Anomalies

Typical examples of fields of the resulting anomalies of η' and T' as they result from the 10-day period July 12–21, 1996 (T/P repeat cycle 141) are shown in Fig. 1. Time-series of both fields are given in Fig. 2 for a few representative locations in the Pacific Ocean. The figures show a striking agreement in the spatial and temporal structures of positive and negative T' and η' anomalies with observed SST anomalies of order 1°C. If representing the upper 200 m depth of the ocean, this would be associated with steric changes in SSH, $\eta'_s = \int_{-h}^{0} \alpha(z)T'(z)dz$ (α being the thermal expansion coefficient), of about 2 cm. Over the bulk of the ocean this is approximately observed. However, in

several regions, noteably the Southern Ocean, SSH changes are much larger, suggesting that processes other than just upper ocean heat content changes are influencing observed changes in sea level there.

Point-wise cross-correlation coefficients between the two anomaly fields were computed over the first 4 years of data, thus excluding the 1997-98 El Niño (Fig. 3a). Correlations of up to 0.6 are found over large parts of the world oceans, most notably the equatorial Pacific, but also the eastern mid-latitude North Atlantic and part of the South Pacific. Note also the strong negative correlation between both fields south of the Antarctic Circumpolar Current, which was already reported by Stammer (1997).

To test the hypothesis that the general circulation is manifested in T' primarily during winter when the mixed-layer extends to great depth, we divided the data into two sets: one consisting of all data northward of 50°S (leaving out the region around the Antarctic Circumpolar Current) and another of all data northward of 20°N (the latter representing boreal seasons) and computed the temporal cross-correlations between T' and η' over those regions as a function of time (Fig. 3b). From a conventional point of view one would expect to see higher correlations in the latter data during boreal winter. However, little such enhancement is seen, and it appears that T' anomalies such as shown in Fig. 1 along wave-like patterns persist throughout the year.

2.2 Global SST spectra

In Fig. 4 we show a global average estimate of the SST frequency-wavenumber spectrum as it follows from 15 years worth of SST data between 1985 and 1997. The spectrum was calculated as described in Wunsch and Stammer (1995) on the basis of a spherical harmonic decomposition of global SST maps. As before, the seasonal cycle was removed from the fields prior to the computations since it would otherwise dominate the figure. Clearly the spectrum is red and depicts highest energy on very long wavelength and

periods. Moreover, the figure illustrates the small amount of energy on small space and time scale which supposedly is due to filter effects of the Reynolds and Smith (1994) objective analysis procedure.

The spectral procedure allows to separate the energy into eastward and westward moving components (see Wunsch and Stammer, 1995 for details) and the global average frequency spectrum, obtained from Fig. 4 by summing over all wavenumbers, is shown in Fig. 5a, together with its east and westward traveling components. The respective global averaged wavenumber spectra are given in Fig. 5b. In both one-dimensional spectra observed energy is roughly divided into equal parts between east and westward propagating anomalies. However, there are some noteworthy exceptions. On long wavelengths enhanced energy associated with the peak around a 5-year period can be found moving eastward. In contrast, the short wavelength part of the spectrum displays persistently more energy moving westward. On periods smaller than the annual cycle the spectral slope is close to -3/2, while on longer periods it is about -2/3.

Frankignoul (1999) interpreted a similar SST frequency spectrum from the North Atlantic in terms of a first order autoregressive Markov process (Hasselmann, 1976; Frankignoul and Hasselman, 1977)

$$\partial_t T' = F'_A - \lambda T', \tag{1}$$

where F'_A represents white-noise atmospheric forcing and λ is a net feedback parameter (being positive for negative feedbacks). The corresponding frequency spectrum can be approximated for $\sigma << \tau_F^{-1}$, by

$$\Phi_T(\sigma) = \frac{\Phi_F(0)}{\sigma^2 + \lambda^2}, \tag{2}$$

where $\Phi_F(0)$ is the level of the 'white' forcing in the frequency band $\sigma << \tau_F^{-1}$.

We have also included in Fig. 5a the spectrum following from (2) which is based on a globally average decay time scale for SST anomalies, λ^{-1}, of the order of 2 months.

Different from what is expected from (2) the global spectrum in Fig. 5a exhibits a red energy distribution up to the longest resolved periods where it thus substantially conflicts with the notion of a simple first order arkov process driven by white atmospheric "noise". Frankignoul (1999) found similar behaviour in spectra for the first two EOF modes from the North Atlantic. An explanation for the red character of the spectrum could be that in our estimate areas are included, such as the tropical latitudes, where the above atmospheric forcing model (1) does not adequately account for the contribution of low-frequency forcing. To investigate to which extend this decay time scale is related to the global averaging procedure, we also computed regional estimates of λ but as e-folding time scales estimated from monthly mean SST anomalies by fitting the autocorrelation function appriopriate for a first order arkov process

$$R_T(\tau) = e^{-\lambda |\tau|} \tag{3}$$

at each individual geographical position (Fig. 6). Observed values $\tilde{R}$ for $\tau > 0$ were weighted by a factor $1/\tau^3$, thus giving most weight to small lags. The figure clearly shows substantial geographical variations in the decorrelation time scale and yields numbers ranging from more than 10 month in low latitudes, down to just a month or shorter at various mid-latitude locations.

While our results from the eastern North Atlantic are in general agreement with previous estimates from this area (e.g. Franignoul et al. 1998), it is interesting to see substantially longer persistence at most low-latitude locations and in the subpolar gyres of the North Pacific and North Atlantic. Wave dynamics may play a significant role in low latitudes. However, in extratropics it can be expected that it is the imprint of winter time atmospheric forcing on the ocean and its slow diffusive-advective adjustment over most of the following year that matters. Thus, although appropriate for the mid-latitude North Atlantic, the non-advective model (1), with F'_A being defined as stochatic atmospheric forcing, is inadequate in explaining a substantial fraction of

(low-frequency) SST variability in many parts of the world oceans, including major current systems and large parts of the North and South Pacific.

To further investigate the causes and the statistical significance of these variations, Fig. 7 depicts examples of T', $\tilde{R}$ and $\tilde{\Phi}_T$ from three different locations. At 30.5°N, 330.5°E, SST is characterized by a fairly short decorrelation time λ^{-1} of 2.1 months, which is close to what is expected due to an atmospheric feedback (damping). The levelling-off of the spectrum at low frequencies is as predicted by (2). Advection is expected to be small here, but may cause somewhat smaller estimates of λ^{-1} for small scale SST anomalies. East of New Zealand at (-40.5°N,180.5°E), where mean circulation maps indicate an intense western boundary current, a similar decay behaviour is found for short time lags, but at longer periods SST is significantly effected by low-frequency processes. This is even more so at equatorial latitudes where the atmospheric forcing is not white but rather determined by ocean variability on much longer time scales. It can be seen that for such conditions the spectrum tends to stay red up to the longest periods resolved.

2.3 Global EOF Analysis of SSH and SST

From Fig. 5 it is apparent that the largest fraction of energy of SST anomalies is found on large spatial scales. To further investigate those large-scale (larger than 1000km) anomalies present in η' and T' and their relation to surface heat fluxes, we performed an empirical orthogonal function (EOF) analysis on the η' and T' fields. A global EOF analysis is complementary to a global spectral description by allowing depiction in the space and time domain of the dominant spatial structures in those fields. The first four modes, representing 39% of the observed variance in SST and 37% in SSH, are shown in Fig. 8. Their temporal structures are presented in Fig. 9. We used data corresponding to the first 156 TOPEX/POSEIDON cycles, thereby excluding the

recent extreme 1997-98 El Niño which would otherwise dominate the entire variability signal (compare e.g. Nerem et al., 1999; Leuliette and Wahr, 1999). In both cases structures are surprisingly close to each other, both in spatial pattern and especially in time expansion. The spatial pattern of EOF 1 show in both cases a strong resemblance with basin scale anomalies as seen in Fig. 1. These first EOF modes are similar to the third EOF modes presented by Nerem et al. (1999) and Leuliette and Wahr (1999). We find here also for higher modes a remarkable agreement in space and time patterns of SSH and SST anomalies. The agreement lies primarily in low frequency oscillations at large spatial scales. Wang and Koblinsky (1997) showed that large scale seasonal changes in SSH in the eastern North Atlantic can be related to surface heat fluxes, in a similar fashion as for SST tendencies (Gill and Niiler, 1973; Yan et al., 1995). The fact that independent investigations have shown similar patterns of global changes in both SST and SSH suggests that atmospheric connections in one way or another effect both fields globally.

3 Small-scale SSH and SST Anomalies

3.1 Time-Longitude Sections

Although anomalous heating (cooling) forces the water column to expand (contract), leading to dynamically passive anomalies in η' fields, much of the low frequency variability in surface elevation appears to be in the so-called first vertical dynamical mode, representing the bulk vertical motion of the deep isotherms (see Wunsch, 1997), and much of that motion in turn can be represented as the propagating free planetary Rossby wave in the ocean. As an example, Jacobs et al. (1994) associated large scale patterns such as those present in Fig. 1 across the North Pacific as being the signature of a first-mode Rossby wave originating from an earlier ENSO event. The fact

that similar patterns clearly emerge also from SST suggest that those η' structures are instead locally driven through air-sea fluxes, or that the SST fields at least to some extend show clear signals of large-scale wave dynamics. Westward traveling signals in the SST anomalies could be an important indication for the impact of ocean currents on observed SST.

To further highlight the latter possibility, we investigate here time longitude sections of both SST and SSH from various extra-tropical latitudes in the North Pacific between 5.5°N and 37.5°N. The zonal sections of sea surface height were obtained from along-track data by space-time optimal interpolation onto the SST 1° grid. The resulting η' sections are characterized by westward propagating, relatively small scale features (top panels of Fig. 10) while SST anomalies (top panels in Fig. 11) are dominated by high-frequent fluctuations on near basin-wide scales. Similar analyses were performed for zonal sections in the South Pacific (Fig. 12) and North Atlantic (Fig. 13). Note that the western part of the 15.5° North Atlantic section is actually an extension into the Caribbean.

In general terms, the characteristics of SST and SSH anomalies from all basins are similar to those in the North Pacific, with SSH being characterized by westward propagating Rossby waves and SST being characterized by relatively faster fluctuations on large zonal scales. However, some westward propagation is clearly evident even in the unfiltered SST anomalies. Note that the 1997-98 El Niño signal is evident both in the North and South Pacific SSH as well as SST fields along the 5.5°N/S and 15.5°N/12.5°S sections.

To gain further insight into the existence of such propagating signals we band-pass filtered both fields using the Loess smoother (Schlax and Chelton, 1992) with high pass filtering in longitude and low pass filtering in time using a cut-off wavelength of 4000 km and cut-off periods of 24, 45, 60 and 90 days respectively for the four sections. This procedure allows for shorter periods at lower latitudes in recognition of the dispersion

relation for linear Rossby wave dynamics. The resulting 'small-scale' anomalies are also displayed in Figs. 10 to 13.

Examples of the large-scale η' and T' residuals (the difference between the original and the small scale fields) from the North Pacific are shown in the middle panels of Figs. 10 and 11. Quite clearly, both fields show substantial large-scale high-frequency fluctuations at various latitudes. Large-scale fast perturbations in SSH have been discussed recently in Stammer et al. (2000) in terms of their relation to fast barotropic fluctuations of the ocean due to time-varying wind stress fields. Consistent with their study, those signals are large in the North Pacific, but are actually present throughout the world ocean. It is quite surprising to see a very similar signal here also in SST suggesting that the barotropic flow component of the ocean has a potential impact on SST

From the small-scale North Pacific anomaly fields (Figs. 10 and 11) several observations can be made:

1) In both fields there are pronounced westward moving anomalies with strikingly similar phase speeds. However, structures are clearly not homogeneous in space and time and are seemingly localized in space for SST at various latitudes.

2) At 5.5°N, propagating features show up in both fields in the eastern part of the section during various periods of the data record, predominantly in late fall. These phenomena look strikingly similar in both fields and show about the same interannual variability in strength and zonal extension. Chelton et al. (1999) discuss the relation of these η' features to Tropical Instability Waves, while Allen et al. (1995) report similar observations from SST data. In agreement with these earlier discussions we observe here apparent interannual modulation of the wave generation, most notably their disappearance during the 1997-98 El Niño. In the South Pacific (Figs. 12) Tropical Instability Waves are observed as well but they appear to be nearly absent in the North Atlantic.

3) Along 15°N, SST anomalies are very pronounced near the eastern boundary, while the SSH appears strong over the entire width of the section. At higher latitude, SSH and SST are both more enhanced on the western side.

The presence of westward propagating Rossby waves in altimetric sea level fields has by now been well documented. Less common have been reports of observed waves in satellite based SST fields. Most early studies have focussed on areas characterized by strong eddy variability and pronounced frontal structures where sharp water mass contrasts reach to the sea surface (Legeckis et al., 1975; Bernstein et al., 1977) whereas others concentrated on the North Atlantic Subtropical Convergence which has been a popular area for extensive field experiments (Voorhis et al., 1976; Halliwell et al., 1991). Rossby wave structures were also reported recently from a regional study of SST and SSH slopes in the North Atlantic (Cipollini et al., 1997). It is obvious from Figs. 1 and 10 to 13, however, that planetary wave patterns are a truly global phenomenon in both T' and η' fields.

Along various sections, most notably 5°N and 5°S in the Pacific, eastward traveling T' anomalies can be detected which seemingly emerge from the western boundary. They suggest reflected planetary wave signal, but are only weakly indicated here in η' (more tuned filtering however will bring out this signature more clearly, as in Fig. 6 in Chelton et al., 1999). A complex atmosphere-ocean interaction is possibly involved in the creation, propagation and ultimately the decay of these anomalies (see also Frankignoul (1985) for more details).

To understand the processes leading to the above SST anomalies, we need to go back to theoretical considerations of processes governing changes of the near-surface SST field (e.g. Frankignoul, 1985). Denoting $T' = T - \overline{T}$ as the anomalies from a seasonally varying mean background state, the evolution of resulting SST anomalies

can be approximated by

$$(\partial_t + \overline{\mathbf{u}}\nabla)\, T' = -\frac{(h\mathbf{u})' \cdot \nabla\overline{T}}{\overline{h}} - \frac{h'}{\overline{h}}\partial_t\overline{T} - \frac{[\Gamma(w_e)w_e(T-T_h)]'}{\overline{h}} + \frac{Q'-Q'_h}{\rho c_p \overline{h}} + \kappa\nabla^2 T', \tag{4}$$

where T and $\mathbf{u}$ represent temperature and horizontal current velocity vertically integrated over the depth h of the mixed layer, w_e denotes the entrainment velocity at its lower boundary, with $\Gamma(w_e) = 1$ for $w_e > 0$ and $\Gamma(w_e) = 0$ otherwise, κ is the eddy diffusivity, representing mixing on all unresolved scales, and the net heat fluxes through the sea surface and through the bottom of the mixed layer are denoted Q and Q_h respectively.

Neglecting mixed-layer depth anomalies and heat fluxes through the mixed-layer base, and approximating the mean temperature gradient by its meridional component, equation (4) can then be rewritten as

$$\partial_t T' + \overline{\mathbf{u}}\nabla T' = -v'_E\, \partial_y\overline{T} - v'_g\, \partial_y\overline{T} - \frac{[\Gamma(w_e)w_e(T-T_h)]'}{\overline{h}} + \frac{Q'}{\rho c_p \overline{h}} + \kappa\nabla^2 T', \tag{5}$$

where the velocity in the first right hand side term in (4) was split into a quasi-geostrophic eddy flow field $\mathbf{u}_g$ and an anomalous time-varying ageostrophic Ekman velocity $\mathbf{u}_E = (\boldsymbol{\tau}' \times \mathbf{k})\,/(\rho f h)$.

To further investigate the impact of the ocean flow field on observed 'small-scale' SST anomalies, we will invoke in the following a simplified heat balance in the form

$$\frac{\partial T'}{\partial t} = -\overline{u}\,\frac{\partial T'}{\partial x} - \frac{g}{f}\frac{\partial\overline{T}}{\partial y}\frac{\partial\eta'}{\partial x} + n_a - \lambda T' \tag{6}$$

i.e. a balance between local changes in T' and advection by the mean current, and meridional advection through a planetary wave field acting on the background temperature gradient in the presence of dissipation, represented by a feedback coefficient λ. The term n_a represents noise originating from neglected atmospheric forcing processes. Note that the meridional geostrophic velocity in (6) was substituted from the zonal

altimetric sea surface slope. Primed quantities are as before anomalies relative to the mean seasonal cycle.

Plotted in Fig. 14 is the rms variability (in time) of the small-scale SSH and SST anomalies, and 15 shows the magnitude of the boreal winter and summer meridional temperature gradients $\partial\overline{T}/\partial y$, evaluated from the monthly mean Levitus and Boyer (1994) SST climatology. Quite clearly and in good agreement with (6), amplitudes of propagating SST anomalies are relatively large in those parts of the sections where the magnitude of the meridional temperature gradient is enhanced, thus giving rise to a more effective anomaly forcing by the surface wave field. This is especially clear for the Pacific at 15.5°north and 12.5°south, and the 15.5 North Atlantic section. At 12.5°S, the SST anomalies are enhanced along both boundaries which is consistent with the increase of SSH variability towards the west and the large meridional temperature gradient on the eastern side (at least during a large fraction of the year). Something similar is observed at 25.5°in the North Atlantic. For the Pacific 5.5°N and 5.5°S sections, as well as at 3.5°N in the Atlantic we observe a reversal of the temperature gradient as compared to the higher latitude sections, implying an increase of the surface temperature poleward. In the Atlantic this reversal takes place at a longitude of approximately 10°W, which appears to be related to some peculiar behavior of the SST anomalies there (Fig. 13).

It should be noted that we observe no obvious seasonal cycle in the relation between the wave-like patterns in η' and T'. Instead, anomalies exist throughout the year (in some cases they can be followed in the SST data over one or two years) quite independently from any anomalous interaction with the atmosphere.

3.2 Zonal Frequency-Wavenumber Spectra

Zonal frequency-wavenumber power density spectra of SSH and SST were computed from the time-longitude sections of Figs. 10 to 12 by applying a 2D FFT algorithm. We show here their autospectra for the North Pacific (Fig. 16) and South Pacific (Fig. 17). Only those parts of the sections were used were a strong correlation on Rossby wave scales between SSH and SST is suggested by the time-longitude plots. In all cases a minimum length of 50 was required, but the resolved zonal wavenumbers differ slightly between the different sections due to the resulting differing zonal span and the increase in the zonal sampling density with latitude. Positive and negative wavenumbers indicate eastward and westward propagating structures and frequency is defined to be positive. In order to increase the confidence level of the estimates, a moving averaging window over 5 by 5 points was applied in the frequency-wavenumber domain, thereby increasing the number of degrees of freedom for each estimate from 2 to 50 (however, only every 5th frequency and wavenumber estimate is therefore independent).

Quite noteticable along all latitudes is the enhanced energy in both fields near the theoretical first mode dispersion curve (plotted as solid lines) for the first-mode baroclinic Rossby waves corresponding with the respective latitude. The curves are based on the Rossby deformation radius estimates of Chelton et al. (1998). Especially, the maximum energy along 5.5 °N associated with the instability waves coincides with the maximum frequency possible for this mode at the upper turning point of the dispersion relation. The substantial amount of eastward propagating energy in the SST fields is quite obvious from the SST spectra but is lacking from the SSH spectra at most latitudes. Among others, Chelton and Schlax (1996) investigated the agreement of SSH observations with the theoretical Rossby wave dispersion curve, and noted that resolved wavenumber-frequency combinations show a tendency to depart from the dis-

persion curve towards higher frequencies (compare also Zang and Wunsch, 1999). We additionally find here a strikingly similar result for SST data.

Halliwell et al. (1991) noted this energy shift relative to the theoretical dispersion curve in their previous SST analysis of the western North Atlanic which they explain partly in terms of the doppler effect of the mean flow field on the Rossby wave phase speed. To test this suggestion, we have plotted in Figs. 16 and 17 as dashed curves the theoretical dispersion curve which take into account the effect of the mean background flow field. These curves are based on estimates of monthly mean zonal surface velocities from ship drift data (Richardson and Walsh, 1986). While some improvement can be seen for the 15°N and 12.5°S latitudes (and especially the 15°N North Atlantic section, not shown), the estimated effect of the mean flow field does not seem to generally remove the discrepancy between the observed and theoretical energy distribution.

Although the accuracy of the mean flow velocity estimates which we use here is debatable, it seems plausible that the shapes of the observed energy spectra are largely determined through a mixed layer temperature model that is forced by anomalous geostrophic currents as in (6). In that case the relation between the autospectra of SST, $\tilde{\Phi}_T$, and SSH, Φ_η, can be described using the zonal-time Fourier transform of that equation (see also Frankignoul and Reynolds, 1983; Halliwell, 1991):

$$\tilde{\Phi}_T(k,\sigma) = \frac{\alpha^2 k^2}{\sigma^2 + \lambda^2}\Phi_\eta(k,\sigma) + \Phi_a \tag{7}$$

where

$$\alpha = \frac{g}{f}\frac{\partial \overline{T}}{\partial y} \tag{8}$$

The term Φ_a represents white atmospheric noise, and it was assumed that $\overline{u} = 0$. Estimates of $\tilde{\Phi}_T$ for the North Pacific are included as the lower panels in Fig. 16. Although not unlike the spectra of the observed temperature anomalies, the predicted SST power in the North Pacific is found at higher wavenumbers than observed, especially in low latitudes.

To obtain estimates of $\tilde{\Phi}_T$, values of the feedback coefficient λ were chosen such that on average the predicted power densities are comparable with the observed values. As suggested by Rahmstorf and Willebrand (1995), the feedback might depend on the spatial scale and it might then not be possible to find a single coefficient valid for the entire range of wavenumbers resolved here. The used feedback coefficients vary from 22 year^{-1} at 15°N to 53 year^{-1} at 37.5°N. These values are higher then may be expected for purely atmospheric feedback. Halliwell at el. (1991) suggested that these values compensate for unmodeled mixing effects which result in a fairly strong damping of SST anomalies.

3.3 Coherence Spectra

The squared coherence, phase lag and gain between SSH and SST, computed from the cross-spectra for each section, are shown in Fig. 18. As mentioned earlier, the phase difference between SSH and SST might give insight into the linking mechanism between both fields. In addition, the squared coherence can be interpreted as the fraction of variance in SST that can be explained as a linear function of SSH. It is in effect an indication of the validity of (6).

The highest coherence values are found at 5.5°N for the frequency band corresponding to the Tropical Instability Wave regime which dominates the (small scale) energy spectrum at this latitude. The squared coherency reaches maximum values of more than 0.8 for a few frequency-wavenumber combinations, implying that more than 80% of the observed SST variance can be explained as a linear function of SSH. The phase difference is close to 180° (a mean of 166°) for (k, σ) combinations where the squared coherency is larger than 0.7.

At 15.5°N, significant coherence values with a maximum larger than 0.6 are found for waves with periods of about half a year and wavelengths of approximately 900 km.

Reduced coherence values are found for the two northernmost North Pacific sections, with maximum values close to 0.5 for 37.5°N. Coherences between SSH and SST are generally lower in the South Pacific but show the same decreasing tendency poleward.

ost noticeable in both the North and South Pacific phase lags is the difference between the 5.5° north and south sections and the other three sections. As in the North Pacific, a phase difference of nearly 180° is found at 5.5°S for frequency-wavenumber combinations associated with the Tropical Instability Wave regime. It can be seen from Fig. 15 that the 180° phase lag for these sections is accompanied by a reversal of the meridional temperature gradient. This phase lag difference with the other sections can not be explained in the framework of an SST variability forced by vertical flow, which would result in largely identical phase signatures for all the sections, and instead points towards horizontal advection as the primary forcing mechanism. The phase lag between SSH and SST for the other sections appears to decrease with increasing latitude. In the North Pacific decrease is observed from about 70° at 15.5°N to almost 0° at 37.5°N. For the three southernmost sections the phase lag of SST with respect to SSH yieds (from north to south) 29°, 26°and 15°, respectively.

The observed gain and phase lags (Fig. 18) can be compared with those predicted by (7). The associated gain and phase of the transfer function are given by:

$$G(k,\sigma) = \frac{|\alpha k|}{(\sigma^2 + \lambda^2)^{1/2}}, \tag{9}$$

and

$$\Theta(k,\sigma) = \tan^{-1}\left(\frac{\lambda}{\sigma}\right). \tag{10}$$

(If $\alpha k < 0$ then π should be added to the phase.) It can be seen from (10) that the presence of feedback mechanisms introduces a phase lag between SST and SSH which would otherwise be zero. Observed gain and phase values at those (k,σ) combinations where the highest coherence was observed, together with relations (9) and (10), were

used to infer appropriate values for the feedback coefficient λ. Values computed using the gain function were generally higher than those obtained using the phase relation, and large differences between the two estimates are possible. We present values obtained for the North Pacific. At 15°N the resulting phase-based estimate of 22 year^{-1} agrees well with the estimate from the previous section. At 5.5°N a value of 15 year^{-1} is found, while at 25.5°N and 37.5°N we obtain values of 52 year^{-1} and 31 year^{-1} respectively, suggesting a more effective damping towards higher latitudes.

A possible explanation for the decrease in coherence between SSH and SST at higher latitudes is the decrease in first-mode baroclinic wave speed. For low forcing frequencies other processes which have largely been neglected here, such as advection by the mean current, entrainment, recurrence, seasonal modulation, mixed-layer depth variability, or even mass-redistribution, might become important. The atmospheric forcing model (1) should become more appropriate at higher latitudes, thus increasing the noise, and further decreasing the coherence between SST and SSH. Goodman and Marshall (1999) discuss the coupling mechanism between SST and the oceanic stream function Ψ supported by their analytical atmosphere-ocean model. They suggest that a maximum in SST should be observed at the maximum in Ψ (depressed thermocline, or raised sea level), and that slow propagating waves should create larger SST anomalies. This is what appears to be observed for the mid-latitude sections where we find small phase differences at low wavenumbers and frequencies.

4 Scaling Arguments

Obviously the agreement between T' and η' is good but not complete, and mechanisms other than the advection of the mean temperature by the eddy flow field must contribute in the total balance as well. In the following we will use scaling arguments to estimate the relative importance of other terms in the equation of the mixed-layer

temperature (5) on 'small' scales. To do so, we inferred the dominant spatial and temporal scales of interest from the wavenumber-frequency power spectra (Figs. 16 and 17) to be typically $k/2\pi \sim 1/1500$ cyc km^{-1} and $\sigma/2\pi \sim 2$ cyc year^{-1} for the three northernmost sections. Values differ slightly with latitude but seperate estimates for the three sections did not significantly alter the results of the analysis presented here. Typical amplitudes for SST and SSH of the order of $\eta' \sim 15$ cm, $T' \sim 0.75$°C are found from the filtered time-longitude plots. onthly mean meridional temperature gradients and mixed-layer depths were computed from Levitus and Boyer (1994) temperature and Levitus et al. (1994) salinity climatologies which yield $\partial_y \overline{T} \sim 5 \cdot 10^{-6}$°C m^{-1} and $\overline{h} \sim 60$ m. Typical mean velocities $(\overline{u}, \overline{v})$ are assumed to be on the order of 10 cm/s.

In agreement with the previous discussion we find that advection by anomalous geostrophic currents associated with Rossby waves is of the same order as the observed local change ($\sigma T' \sim 3 \cdot 10^{-7}$°C s^{-1}), i.e., $\sigma\, T' \sim g\, k\, \eta\, \partial_y \overline{T}/f$. At the same time we find that $\sigma \sim k\, \overline{u}$ which implies that the advection of SST anomalies by the zonal mean (geostrophic and Ekman) current is of the same order as typical local temperature changes. In other words, for the lower to mid-latitudes, the mean current velocity $\overline{u}$ is of the same order as the wave speed σ/k. However, near major boundary currents and at high latitudes, the mean current can become larger.

Eddies and waves may also change the SST by vertical advection across the mixed-layer base. Assuming a temperature jump across the mixed layer base of $\Delta T = 0.5$°C (this corresponds with a density change of approximately 0.125 kg m^{-3}, commonly used to define the mixed-layer depth), and assuming furthermore that baroclinic waves are associated with vertical oscillations of the thermocline on the order of $A \sim 100$ m (such that the vertical velocity w' within the thermocline will vary with an amplitude σA) the ratio of the horizontal to vertical advection terms is then approximately $\left(g\, k\, \eta\, \partial_y \overline{T}/f\right) / \left(A\, \sigma\, \Delta T/\overline{h}\right) \sim 1$, implying that it is both the horizontal advection and the vertical movement of the isopycnals which contribute to the observed SST

variability. However, this is most likely an upper bound, since the amplitude of vertical oscillation at the depth of the mixed-layer base is very likely smaller than the one assumed above (amplitudes decrease towards the surface with a factor of order $10^2 - 10^3$). Stevenson (1983) found that for typical ODE conditions SST modifications due to vertical advection had an amplitude of about 0.35°C. With the scaling values assumed here, and in agreement with estimates by Frankignoul (1985), we find that the amplitude of SST anomalies induced by horizontal advection would be about 1.13°C, thus more than 3 times larger, a conclusion which is consistent with the observed phase differences between SSH and SST.

With a small-scale zonal wind stress anomaly of $\tau \sim 2.5 \cdot 10^{-2}$ N m^{-2}, the term representing anomalous Ekman currents acting on the mean temperature gradient is $(\tau\, \partial_y \overline{T})/(\rho\, f\, \overline{h}) \sim 2.5 \cdot 10^{-8}$°C s^{-1}, which is about an order of magnitude smaller then the local change. Similarly, based on characteristic wind stress curl amplitudes in NCEP fields ($curl(\tau) \sim 1 \cdot 10^{-7}$N m^{-3}) we find that the vertical Ekman pumping term (with values for ΔT and $\overline{h}$ as used earlier) $w_E\, \Delta T/\overline{h} \approx curl(\tau)\, \Delta T/(\rho\, f\, \overline{h}) \sim 1 \cdot 10^{-8}$.

In summary, we obtained estimates of individual terms of (5) according to $O(10^{-7})+O(10^{-7}) = O(10^{-8})+O(10^{-7})+O(10^{-8})+O(10^{-7})+$diffusion. This is also demonstrated in Fig. 19 which displayes time-longitude sections along 25.5°N in the North Pacific of the various terms in the temperature equation (5): 1) local SST changes, 2) advection of the mean SST by anomalous geostrophic current, 3) advection by anomalous horizontal Ekman currents, 4) anomalous Ekman pumping, and 5) heat fluxes. All fields were filtered prior to the compilation using the same filter parameters that were used for the SSH and SST fields. We used the time averaged mixed-layer depths and temperature gradients, since seasonally varying terms were found to produce seasonal modulations which are not seen in the temperature or in the temperature tendency. The heat flux field is found to contain propagating signal with a signature very similar to that of the temperature field itself. This suggests that rather than a forcing term, heat fluxes on

these scales act as a feedback mechanism in proportion to the magnitude of the SST anomaly as in (1) with

$$\lambda = \frac{1}{\rho c_p \overline{h}} \frac{\partial Q'}{\partial T'}$$

Focussing on the propagating signal, we find from Fig. 19 a heat flux feedback of 30-40 W m^{-2}, which for $T' \sim 0.6°C$ leads to a decay time λ^{-1} of approximately 30-40 days. The atmospheric feedback found here is at the high end of estimates for large scale SST anomalies and is not inconsistent with previous indications (Frankignoul, 1985) that smaller anomalies have less persistence.

We must conclude that at mid-latitudes no single forcing term can account for all low-frequency 'small-scale' SST variability. Instead, a rather complex combination of horizontal and vertical advection and damping terms is responsible for setting observed SST changes, whith Ekman terms apparently being of lesser importance. There remain uncertainties in the estimation of some of these terms due to their dependence on parameters such as ΔT and $\overline{h}$, while small-scale mixing has been ignored altogether.

5 Summary

Previously it was assumed that SST observations bare little or no resemblance to processes in the interior (subsurface) ocean. It is therefore remarkable to see how much resemblance can actually be found between SST and SSH fields. Our analysis of phenomena outside the seasonal frequency indicate that large-scale anomalies of open-ocean SST and SSH variability seem to result primarily from surface-driven steric effects rather than from advective coupling of the mixed layer with the interior ocean (see also Nerem et al., 1999; Leuliette and Wahr, 1999). This is in agreement with results which suggest that large scale mid-latitude changes in SST and SSH are primarily due to local heat exchanges with the atmosphere (Frankignoul and Reynolds, 1983; Cayan, 1992; Yan et al., 1995; Chambers et al., 1997; Wang and Koblinksy, 1997).

Typically one third of the rms SST variability outside the seasonal cycle can be associated with wavelengths smaller than 1000km and at many latitudes small-scale features are closely related to free first-mode baroclinic Rossby waves. These waves create a signature in the SST field which in some cases can be followed for over a year, thus exceeding persistence times of atmospherically forced anomalies at mid-latitudes (Frankignoul et al., 1998). Dynamically coupled anomalies in SSH and SST have been reported earlier in limited regions (Halliwell et al., 1991; Cipollini et al., 1997). We show here that these features can be detected in all ocean basins extending from near equatorial to mid-latitudes. It appears that a necessary condition for the existence of Rossby wave-like SST anomalies is the existence of a non-zero meridional background temperature gradient which is acted on by the wave's meridional velocity component. However, this process for dynamically creating SST anomalies becomes less efficient towards high latitudes, where Rossby wave phase speeds decrease substantially thus allowing for more efficient atmospheric damping of induced SST anomalies, and where changes in the wind will also result in changes in local oceanic dynamics, heat flux divergences and re-distribution of mass.

Damping coefficients estimated from the phase lags between SSH and SST anomalies result in values of 20-30 year^{-1} with some estimates far exceeding these numbers. These numbers are much larger than those generally assumed for atmospheric feedback in mid-latitudes (e.g., Frankignoul et al. 1998), and Halliwell et al. (1991) suggested that they rather represent the damping effect of ocean mixing processes. From our analysis there is evidence that there is a significant coupling in the horizontal between the surface mixed layer and the underlying layers through oceanic currents associated with a baroclinic wave field. oreover, Fig. 7 suggests a significant influence of low-frequency modulation of SST by ocean variability for all major current systems.

A global (area-weighted) average of local correlation scales in Fig. 6 yields an estimate of 3 months. This is slightly larger than the global mean value estimated from

the spectra given in Fig. 5a, possibly because the fit of the auto-correlation functions is partly influenced by the low-frequency energy, while the spectrum was chosen to match only the high-frequency part. Both numbers are considerably larger than those obtained for the small-scale transient anomalies which instead yield a decay-timescales between 0.2 and 0.3 months – roughly an order of magnitude smaller than those found for the large-scale anomalies.

Different from the Halliwell et al. (1991) assertion of ocean mixing, Rahmstorf and Willebrand (1995) used a scale-dependent parameterization of the air-sea coupling. Although applicable in a very different context, it is remarkable to find that their choice of inverse coupling coefficients of 0.8 month and 1.6 month for anomalies on spatial scale of 400 km and 1000 km respectively, is strikingly close to the estimates we obtain here from time-longitude plots for feedback on similar scales.

The major conclusion of this paper is that a significant fraction of the low-frequency variability of SST is connected to dynamical processes which extend over the entire oceanic water column. Understanding of the joint evolution of the coupled ocean-atmosphere, which defines much of the climate system, will therefore necessarily require accounting for oceanic circulation structures and variability not now represented in models. As the data sets lengthen and the known or suspected errors in them are removed, a fuller description of the air-sea coupling as a function of position, and of time and space-scales will become possible.

Acknowledgments. Charmain King helped with some of the computations. Helpful discussions with Carl Wunsch and Claude Frankignoul are gratefully acknowledged. D.S. was supported by contract JPL-68571, and by contract NAGW-7857 with NASA. O.L. acknowledges support by the Danish Research Council, Program in Earth Observation and the hospitality of EAPS, MIT. Contribution to GEOSONAR and WOCE.

References

1. Allen, M. R., S. P. Lawrence, M. J. Murray, C. T. Mutlow, T. N. Stockdale, D. T. Llewellyn-Jones and D. L. T. Anderson, 1995: Control of instability waves in the Pacific, *Geophys. Res. Letters*, 22, 2581–2584.

2. Bernstein, R. L., L. Breaker, and R. Whritner, 1977: California Current eddy formation: ship, air and satellite results, *Science*, 1995, 353–359.

3. Cayan, D. R., 1992: Latent and sensible heat flux anomalies over the northern oceans: Driving the sea surface temperature, *J. Phys. Oceanogr.*, 22, 859–881.

4. Chambers, D. P., B. D. Tapley and R. H. Stewart, 1997: Long-period ocean heat storage rates and basin-scale heat fluxes from TOPEX, *J. Geophys. Res.*, 102, 10,525-10,533.

5. Chelton, D. B., and M. G. Schlax, 1996: Global observations of oceanic Rossby waves, *Science*, *272*, 234–238.

6. Chelton, D. B., M. G. Schlax, J. M. Lyman, and R.A de Szoeke, 1999: The latitudinal structure of monthly variability in the tropical Pacific, submitted to J. Phys. Oceanogr.

7. Chelton, D. B., R. A. deSzoeke, M. G. Schlax, K. El Naggar and N. Siwertz, 1998: Geographical variability of the first baroclinic Rossby radius of deformation, *J. Phys. Oceanogr.*, 28, 433–460.

8. Cipollini, P., D. Cromwell, M.S. Jones, G. D. Quartly, and P.G. Challenor, 1997, Concurrent altimeter and infrared observations of Rossby waves propagating near 34°N in the Northeast Atlantic. *Geophys. Res. Letters*, 24,885–892.

9. Czaja, A. and C. Frankignoul, 1999: Influence of North Atlantic SST on the atmospheric circulation, *Geophys. Res. Letters*, 26, 2969–2972.

10. Deser, C.M., A. Alexander and M.S. Timlin, 1998: Upper-ocean thermal variations in the North Pacific during 1970-1991. *J. Clim.*, 9, 1840–1855.

11. Frankignoul, C., 1985: Sea surface temperature anomalies, planetary waves, and air-sea feedback in the middle latitudes,. *Rev. of Geophys.*, 23, 357–390.

12. Frankignoul, C., 1999: Sea surface temperature variability in the North Atlantic on monthly to decadal time scales. In "Beyond El Nino: Decadal and interdecadal Climate Variability Ed. A. Navarra. Springer-Verlag, 25-47.

13. Frankignoul, C. and K. Hasselmann, 1977: Stochastic climate studies, II: Application to sea-surface temperature variability and thermocline, *Tellus*, 29, 284–305.

14. Frankignoul, C. and R. W. Reynolds, 1983: Testing a dynamical model for mid-latitude sea surface temperature anomalies, *J. Phys. Oceanogr.*, 13, 1131–1145.

15. Frankignoul, C., A. Czaja, and B. L'Heveder, 1998: air-sea feedback in the North Atlantic and surface boundary conditions for ocean models, *J. Climate*, 11, 2310-2324.

16. Gill, A.E., and P.P Niiler, 1973: The theory of the seasonal variability in the ocean, *Deep Sea Res.*, **20**, 141–177.

17. Goodman, J., and J. Marshall, 1999: A model of decadal middle-latitude atmosphere-ocean coupled modes. *J. Climate*, 12, 621-641.

18. Halliwell, G.R.,Jr., Y. J. Ro, and P. Cornillon, 1991: Westward-propagating SST anomalies and baroclinic eddies in the Sargasso Sea, *J. Phys. Oceanogr.*, 21, 1664–1680.

19. Jacobs, G., H.E. Hurlburt, J.C. Kindle, E.J. Metzger, J.L. Mitchell, W.J. Teague, and A.J. Wallcraft, 1994: Decadal-scale trans-Pacific propagation and warming effects of an ño anomaly, *Nature*, 370, 360–363.

20. Kushnir, Y., 1994: Interdecadal variations in North Atlantic sea surface temperature and associated atmospheric conditions, *J. Climate*, 7, 141–157.

21. Kushnir, Y., and I. M. Held, 1996: Equilibrium atmospheric response to North Atlantic SST anomalies. *J. Climate.*, 9, 1208–1220.

22. Legeckis, R.V., 1975: Application of synchronous meteorological satellite data to the study of time dependent sea surface temperature changes along the boundary of the Gulf stream, *Geophys. Res. Letters*, 2, 435–438.

23. Leuliette, E.W., and J. M. Wahr, 1999: Coupled pattern analysis of sea surface temperature and TOPEX/POSEIDON sea surface height, *J. Phys. Oceanogr.*, 29, 599–611.

24. Levitus, S. and T. P. Boyer: World Ocean Atlas 1994, Volume 4: Temperature, vol. NOAA Atlas NESDIS 3, 117 pp., U.S. Dept. Comm., Washington DC.

25. Levitus, S., R. Burgett and T. P. Boyer: World Ocean Atlas 1994, Volume 3: Salinity, vol. NOAA Atlas NESDIS 3, 97 pp., U.S. Dept. Comm., Washington DC.

26. Nerem, S., D. P. Chambers, E. W. Leuliette, G. T. Mitchum and B. S. Giese, 1999: Variations in global mean sea level associated with the 1997–1998 ENSO event: Implications for measuring long term sea level change, *Geophys. Res. Letters*, 26, 3005–3008.

27. Rahmstorf, S., and J. Willebrand, 1995: The role of temperature feedback in stabilizing the thermohaline circulation. *J. Phys. Oceanogr.*, 25, 787–805.

28. Reynolds, R. W., and T. M. Smith, 1994: Improved global sea surface temperature analysis using optimum interpolation. *J. Climate*, 7, 929–948.

29. Richardson, P. L., and D. Walsh, 1986: Mapping climatological seasonal variations of surface currents in the tropical Atlantic using ship drifts, J. Geophys. Res., 91, 10537–10550.

30. Schlax, M. G. and D. B. Chelton, 1992: Frequency domain diagnostics for linear smoothers, *J. Am. Stat. Assoc.*, 87, 1070–1081.

31. Stammer, D., 1997: Steric and wind-induced changes in large-scale sea surface topography observed by TOPEX/POSEIDON, *J. Geophys. Res.*, 20,987–21,010.

32. Stammer, D., C. Wunsch, and R. Ponte, 2000: De-Aliasing of Global High Frequency Barotropic Motions in Altimeter Observations, *Geophysical Res. Letters*, in press. .

33. Stammer, D. and C. Wunsch, 1994: Preliminary assessment of the accuracy and precision of TOPEX/POSEIDON altimeter data with respect to the large scale ocean circulation. *J. Geophys. Res.*, 99, 24584–25,604.

34. Stevenson, J. W., 1983: The seasonal variation of the surface mixed-layer response to the vertical motions of linear Rossby waves, *J. Phys. Oceanogr.*, 13, 1255–1268.

35. Voorhis, A. D., E. H. Schroeder and A. Leetmaa, 1976: The influence of deep mesoscale eddies on sea surface temperature in the North Atlantic subtropical convergence, *J. Phys. Oceanogr.*, 6, 953–961.

36. Wang, L. and C. Koblinsky, 1997: Can the Topex/Poseidon altimetry data be used to estimate air-sea heat flux in the North Atlantic?, *Geophys. Res. Letters*, 24, 139-142.

37. Wunsch, C., 1997: The vertical partition of oceanic horizontal kinetic energy and the spectrum of global variability, *J. Phys. Oceanogr.*, 27, 1770–1794.

38. Wunsch, C. and D. Stammer, 1995: The global frequency-wavenumber spectrum of oceanic variability estimated from TOPEX/POSEIDON altimeter measurements, *J. Geophys. Res.*, 100, 24,895–29,910.

39. Yan, X.-H., P. P. Niiler, S. K. Nadiga, R. H. Stewart and D. R Cayan, 1995: Seasonal heat storage in the North Pacific: 1976–1989, *J. Geophys. Res.*, 100, 6899–6926.

40. Zang, X. and C. Wunsch, 1999: The observed dispersion relationship for North Pacific Rossby wave motions, *J. Phys. Oceanogr.*, 29, 2183–2190.

Figure Captions

1. **Fig. 1**: Instantaneous (10-day averaged) maps of sea surface height and SST anomaly fields from the period July 12–21, 1996 (T/P repeat cycle 141). Both fields represent off-seasonal anomalies, i.e., anomalies relative to a four-year mean seasonal cycle of the data. Additionally they were smoothed in time by a 30-day moving average window, and in space using a Shapiro low-path filter which removes all energy on the 2° grid spacing.

2. **Fig. 2**: Timeseries of T' (solid, red line) and η' (dashed, blue line) from various locations of the Atlantic Ocean. Correlations between the two curves are 0.7, 0.4, 0.71, and 0.01, respectively (from upper left to lower right panel). Note that $4 \times T'$ was plotted for visualization.

3. **Fig. 3a**: Local correlation coefficient between the timeseries of T' and η'.
   Fig. 3b: The correlation coefficient between fields of T' and η' such as shown in Fig. 1 plotted as a function of time. The solid line represents data from north of 20°N, while the dotted line is based on all data north of 50°S.

4. **Fig. 4**: Global frequency - wavenumber spectrum of sea surface temperature, computed from a spherical harmonic expansion.

5. **Fig. 5** (a) Global average frequency spectrum of SST, obtained by summing over all wavenumbers. (b): Global average wavenumber spectrum, obtained by summing over all frequencies.

6. **Fig. 6**: Persistence of sea surface temperature anomalies defined as e-folding decay time, computed for each 1°× 1°grid box from 10-day averages.

7. **Fig. 7**: SST, its auto-covariance and power spectral density for three locations in the mid-latitude North Atlantic, South Pacific and equatorial Pacific.

8. **Fig. 8**: Spatial patterns of the first 4 global EOF modes of sea surface height and temperature, computed from T/P cycles 1-156.

9. **Fig. 9**: Time series of the first 4 EOF modes corresponding to the spatial patterns in Fig. 8.

10. **Fig. 10**: Time - longitude sections of η' along various latitudes in the North Pacific: 5.5°N, 15.5°N, 25.5°N, and 37.5°N.

11. **Fig. 11**: Time - longitude sections of T' along various latitudes in the North Pacific: 5.5°N, 15.5°N, 25.5°N, and 37.5°N.

12. **Fig. 12**: Time - longitude sections of η' and T' along various latitudes in the South Pacific: 5.5°S, 12.5°S, 25.5°S, and 37.5°S.

13. **Fig. 13**: Time - longitude sections of η' and T' along various latitudes in the North Atlantic: 3.5°N, 15.5°N, 28.5°N, and 35.5°N.

14. **Fig. 14** Root-mean-square variability of sea level (red) and temperature (blue).

15. **Fig. 15**: Mean meridional temperature gradient averaged over boreal winter (blue) and summer months (red).

16. **Fig. 16**: Observed frequency - wavenumber power spectral density Φ of sea level (top) and temperature (middle) for each of the four North Pacific sections. The true spectrum lies within $0.62 \cdot \Phi$ and $1.91 \cdot \Phi$ with 95% confidence. The solid line represents the first mode Rossby wave dispersion curve for a zero mean zonal current. The dashed line shows the effect of including a ship-drift based estimate of the annual mean zonal flow. Units are in $\mathrm{cm}^2/(\mathrm{cyc{\cdot}year}^{-1} \cdot \mathrm{cyc{\cdot}1000km}^{-1})$ for SSH and $°\mathrm{C}^2/(\mathrm{cyc{\cdot}year}^{-1} \cdot \mathrm{cyc{\cdot}1000km}^{-1})$ for SST. The bottom panels show the predicted SST power spectral density.

17. **Fig. 17**: As in Fig. 16, but for the South Pacific.

18. **Fig. 18**: Squared coherence, phase lag and gain between SSH and SST for the wavenumber - frequency combinations with the highest significant coherence. The lines again represent the first mode Rossby wave dispersion curves.

19. **Fig. 19**: Time - longitude plots of the 'small-scale' contributions from the different terms in the mixed-layer temperature equation: temperature tendency ($\partial_t T'$), anomalous geostrophic flow field ($-v_g' \overline{T}_y$), Ekman pumping ($-w_e \Delta\overline{T}/\overline{h}$), temperature ($T'$), Ekman transport ($-\mathbf{u}_e \nabla\overline{T}$), and net surface heat flux ($Q'/(\rho c_p \overline{h})$). Units are °C s^{-1}, except for the temperature (°C).

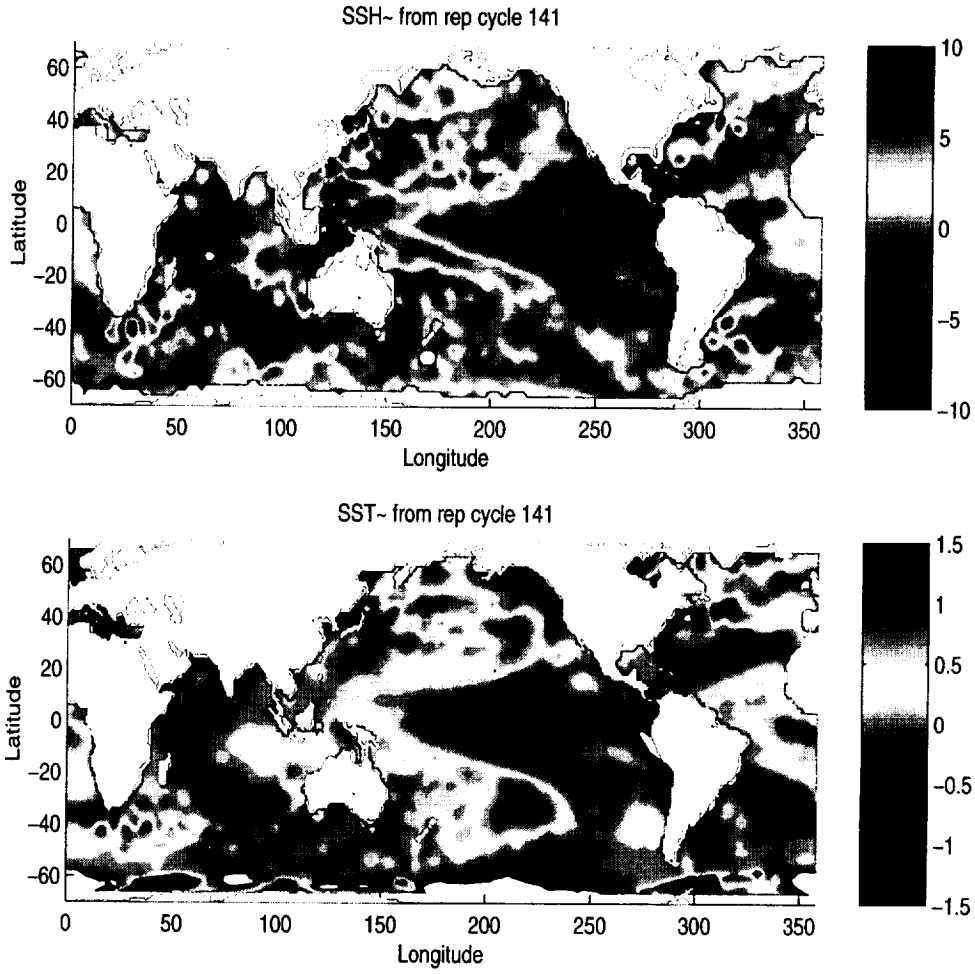
SSH~ from rep cycle 141
Latitude
Longitude
60
40
20
0
-20
-40
-60
0
50
100
150
200
250
300
350
10
5
0
-5
-10
SST~ from rep cycle 141
Latitude
Longitude
1.5
1
0.5
0
-0.5
-1
-1.5

Figure 1:

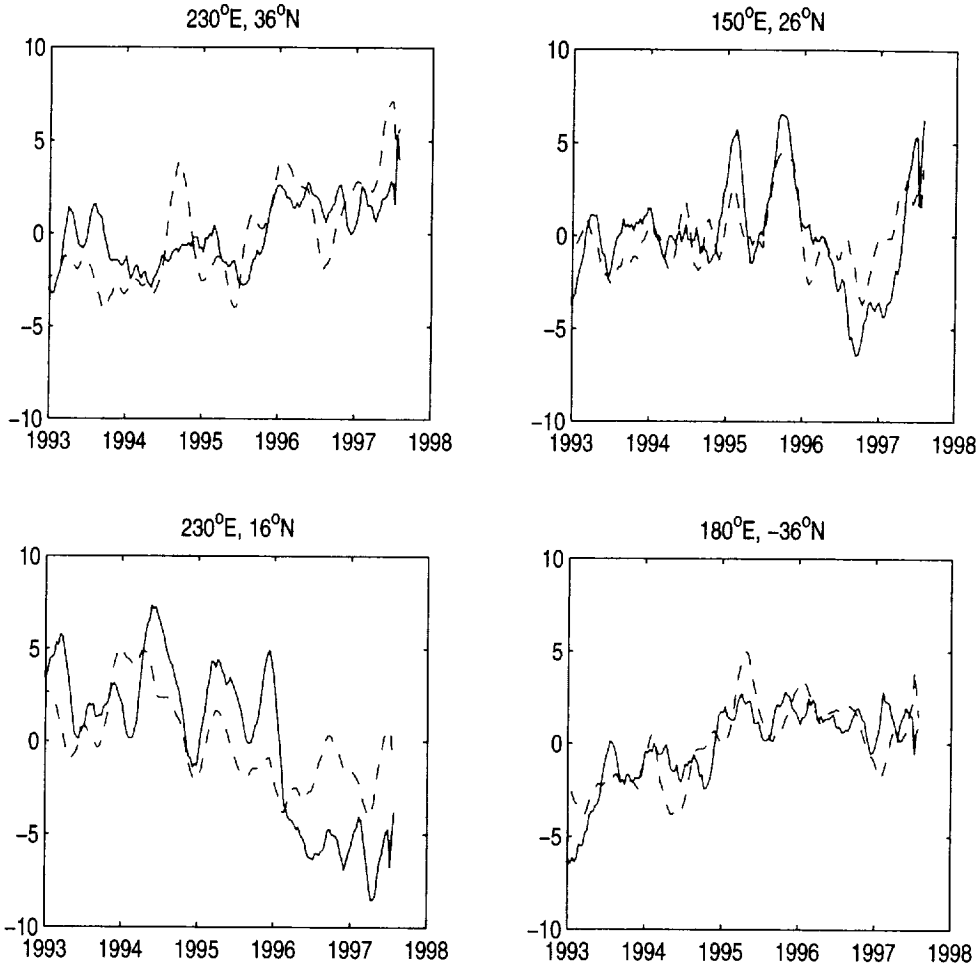
230°E, 36°N
150°E, 26°N
230°E, 16°N
180°E, -36°N
10
5
0
−5
−10
1993
1994
1995
1996
1997
1998

Figure 2:

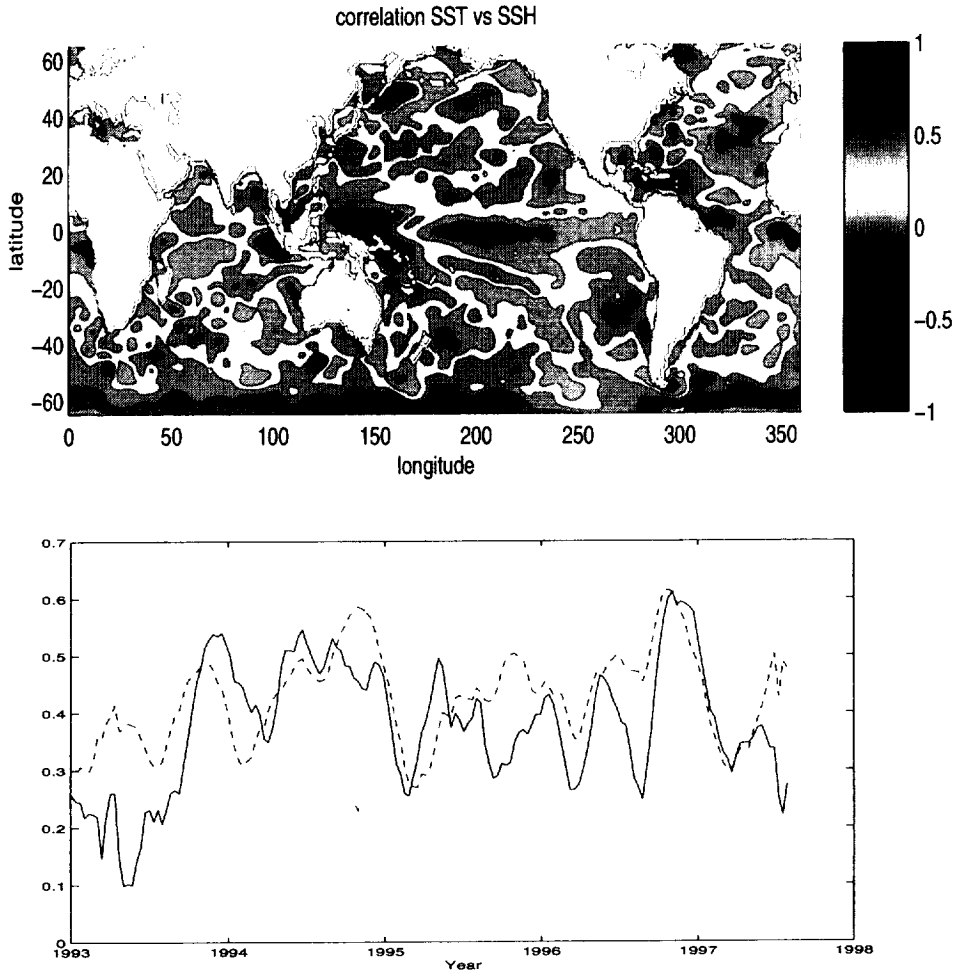
correlation SST vs SSH
latitude
longitude
60
40
20
0
-20
-40
-60
0
50
100
150
200
250
300
350
1
0.5
0
-0.5
-1
0.7
0.6
0.5
0.4
0.3
0.2
0.1
0
1993
1994
1995
1996
1997
1998
Year

Figure 3:

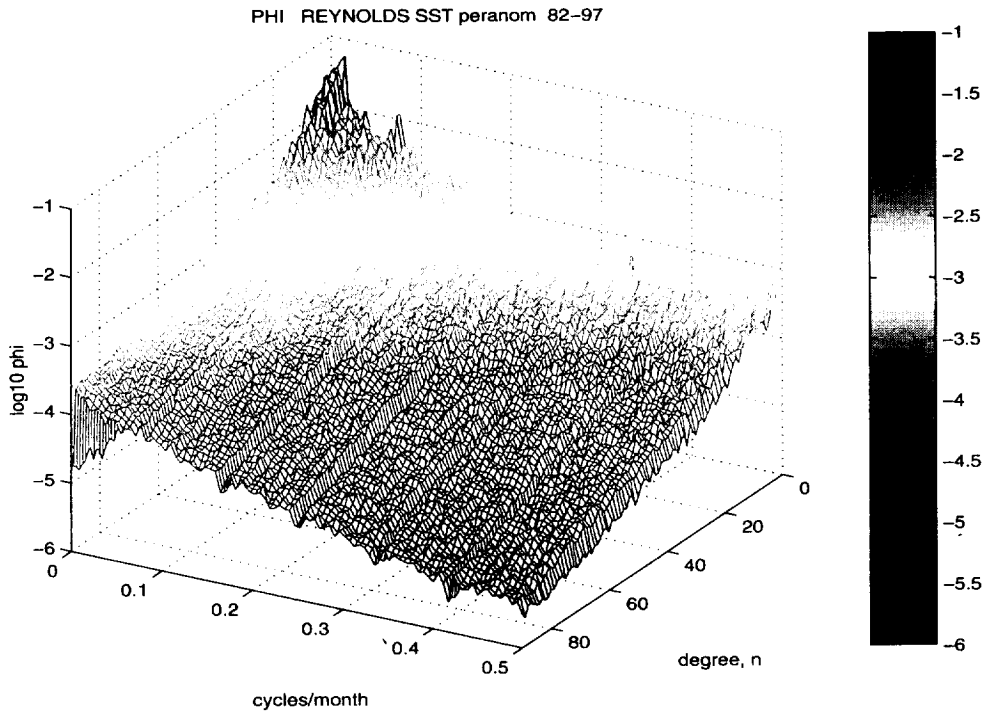
PHI REYNOLDS SST peranom 82-97
log10 phi
-1
-2
-3
-4
-5
-6
0
0.1
0.2
0.3
0.4
0.5
cycles/month
0
20
40
60
80
degree, n
-1
-1.5
-2
-2.5
-3
-3.5
-4
-4.5
-5
-5.5
-6

Figure 4:

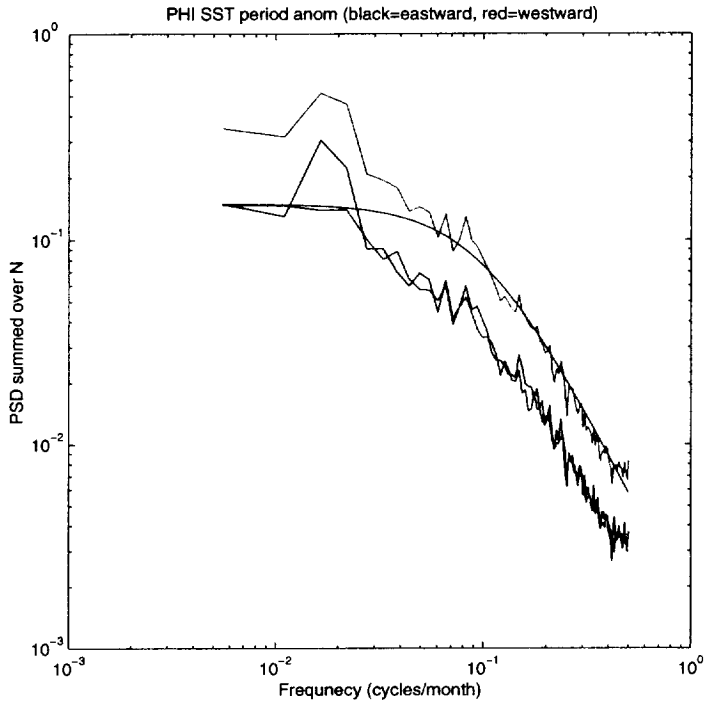
PHI SST period anom (black=eastward, red=westward)
PSD summed over N
Frequnecy (cycles/month)

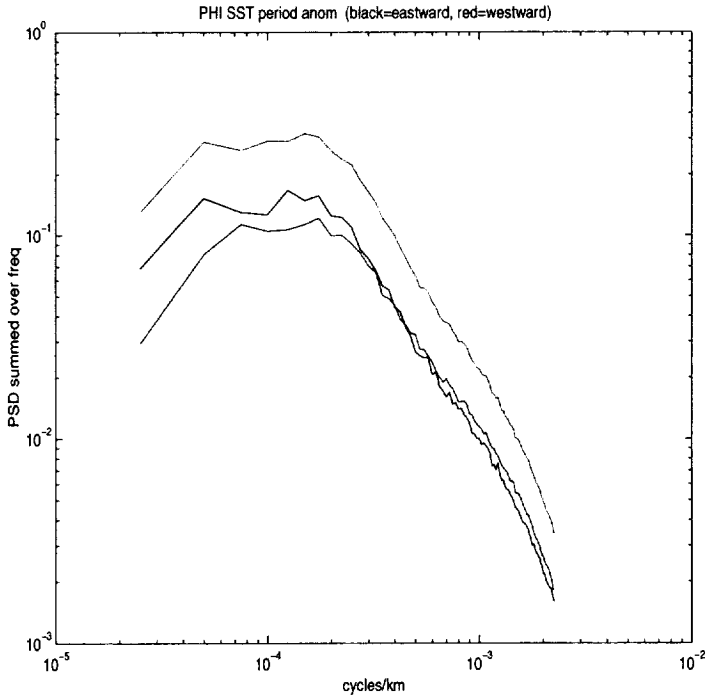
PHI SST period anom (black=eastward, red=westward)
PSD summed over freq
cycles/km

Figure 5:

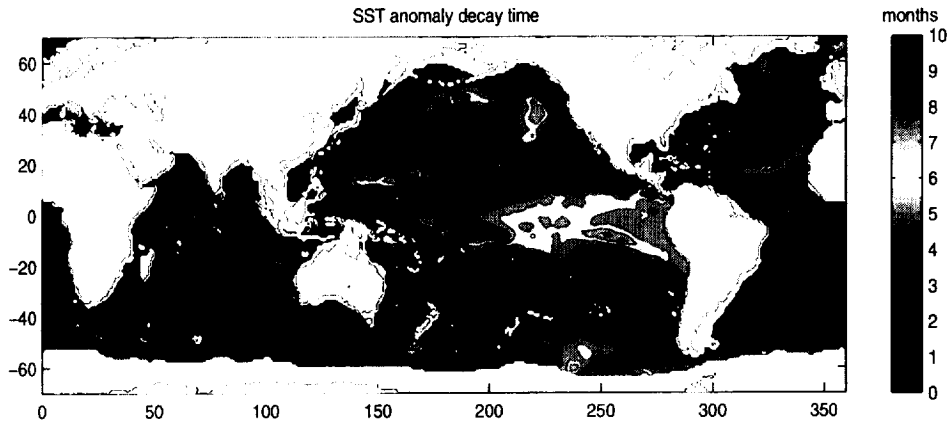
SST anomaly decay time
months
60
40
20
0
-20
-40
-60
0
50
100
150
200
250
300
350
10
9
8
7
6
5
4
3
2
1
0

Figure 6:

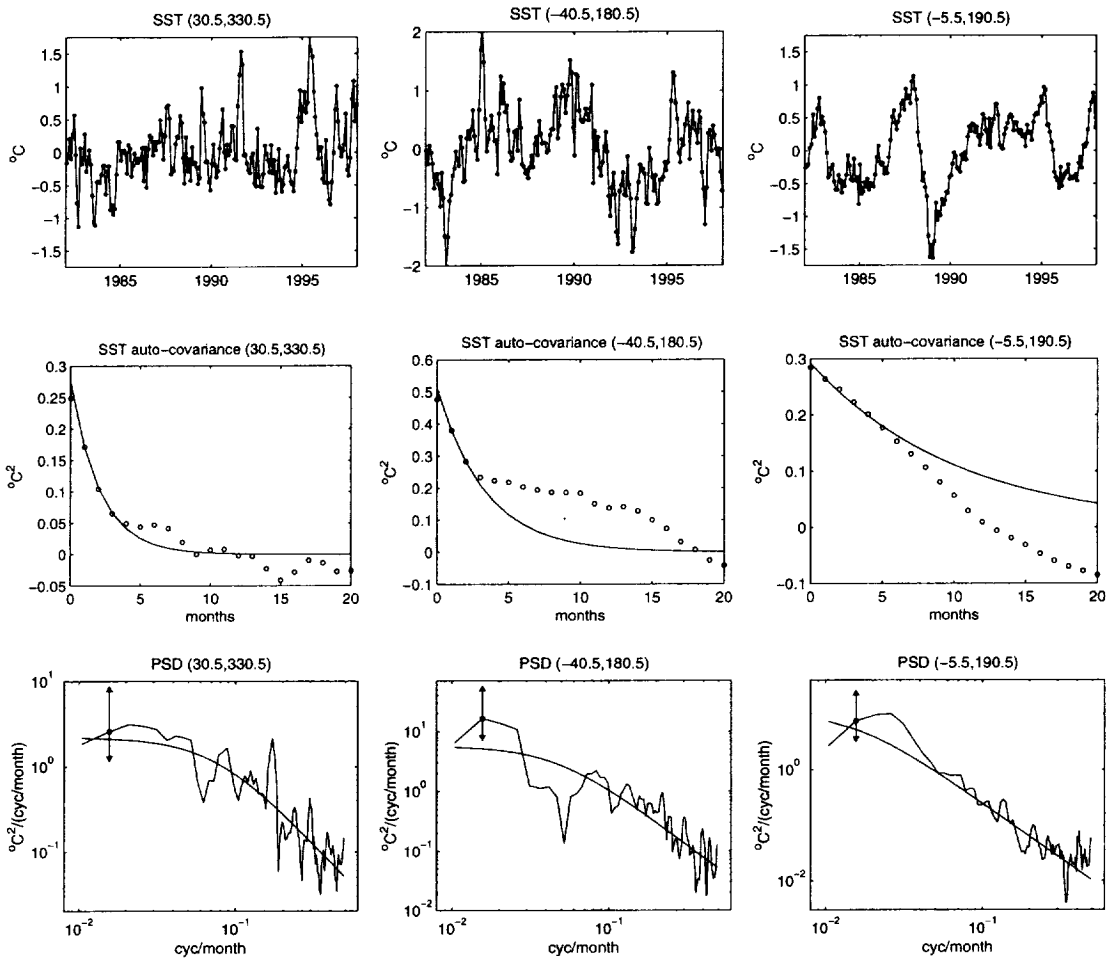
SST (30.5,330.5)
SST (−40.5,180.5)
SST (−5.5,190.5)
°C
1985
1990
1995
SST auto−covariance (30.5,330.5)
SST auto−covariance (−40.5,180.5)
SST auto−covariance (−5.5,190.5)
°C²
months
PSD (30.5,330.5)
PSD (−40.5,180.5)
PSD (−5.5,190.5)
°C²/(cyc/month)
cyc/month

Figure 7:

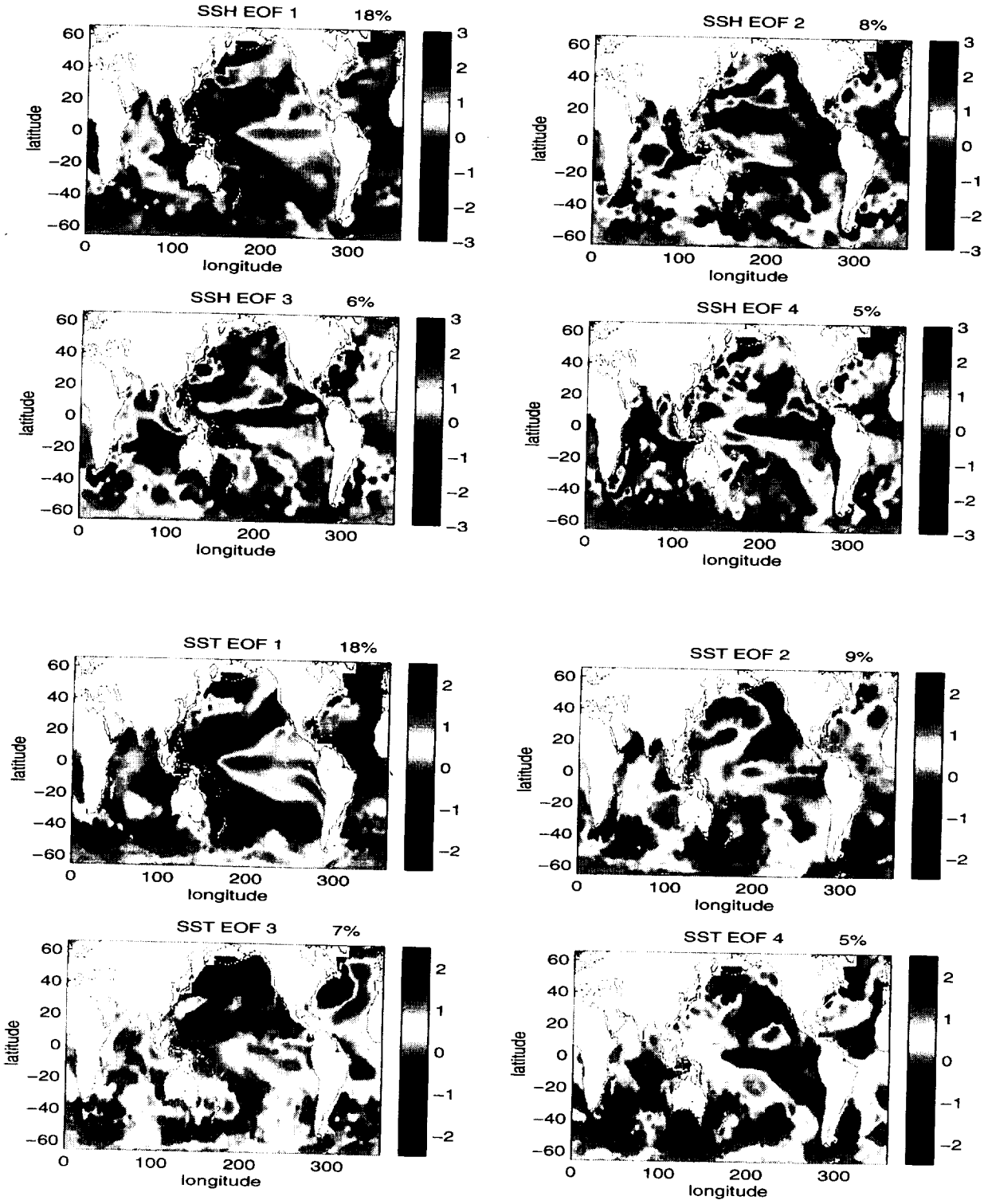
SSH EOF 1
18%
SSH EOF 2
8%
SSH EOF 3
6%
SSH EOF 4
5%
SST EOF 1
18%
SST EOF 2
9%
SST EOF 3
7%
SST EOF 4
5%
latitude
longitude

Figure 8:

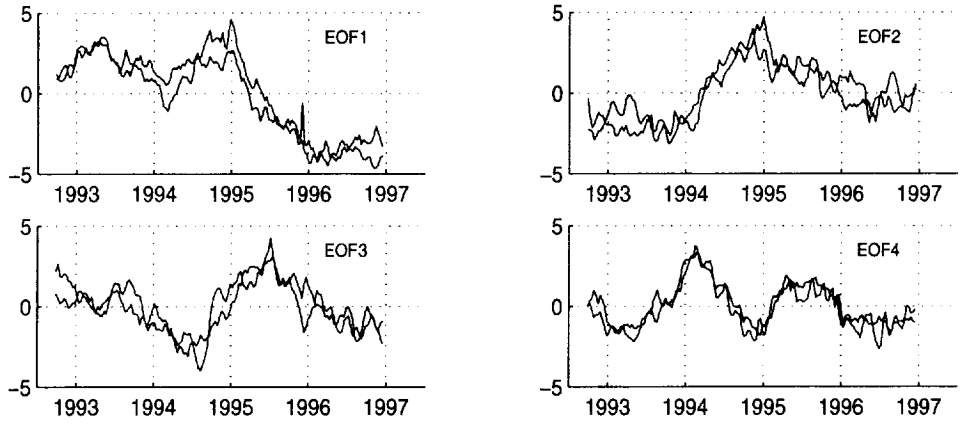

Figure 9:

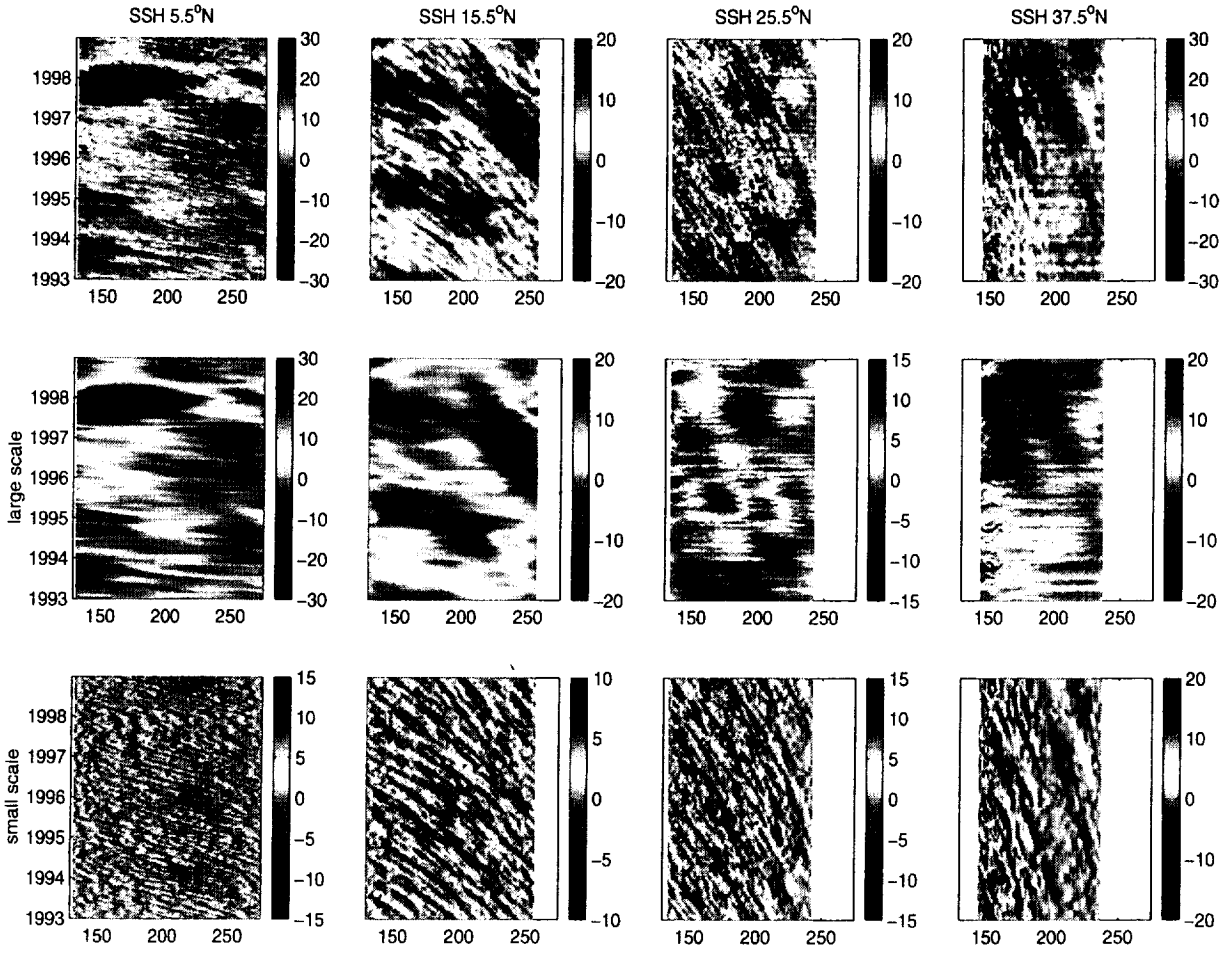
SSH 5.5°N
SSH 15.5°N
SSH 25.5°N
SSH 37.5°N
large scale
small scale
1998
1997
1996
1995
1994
1993
150
200
250

Figure 10:

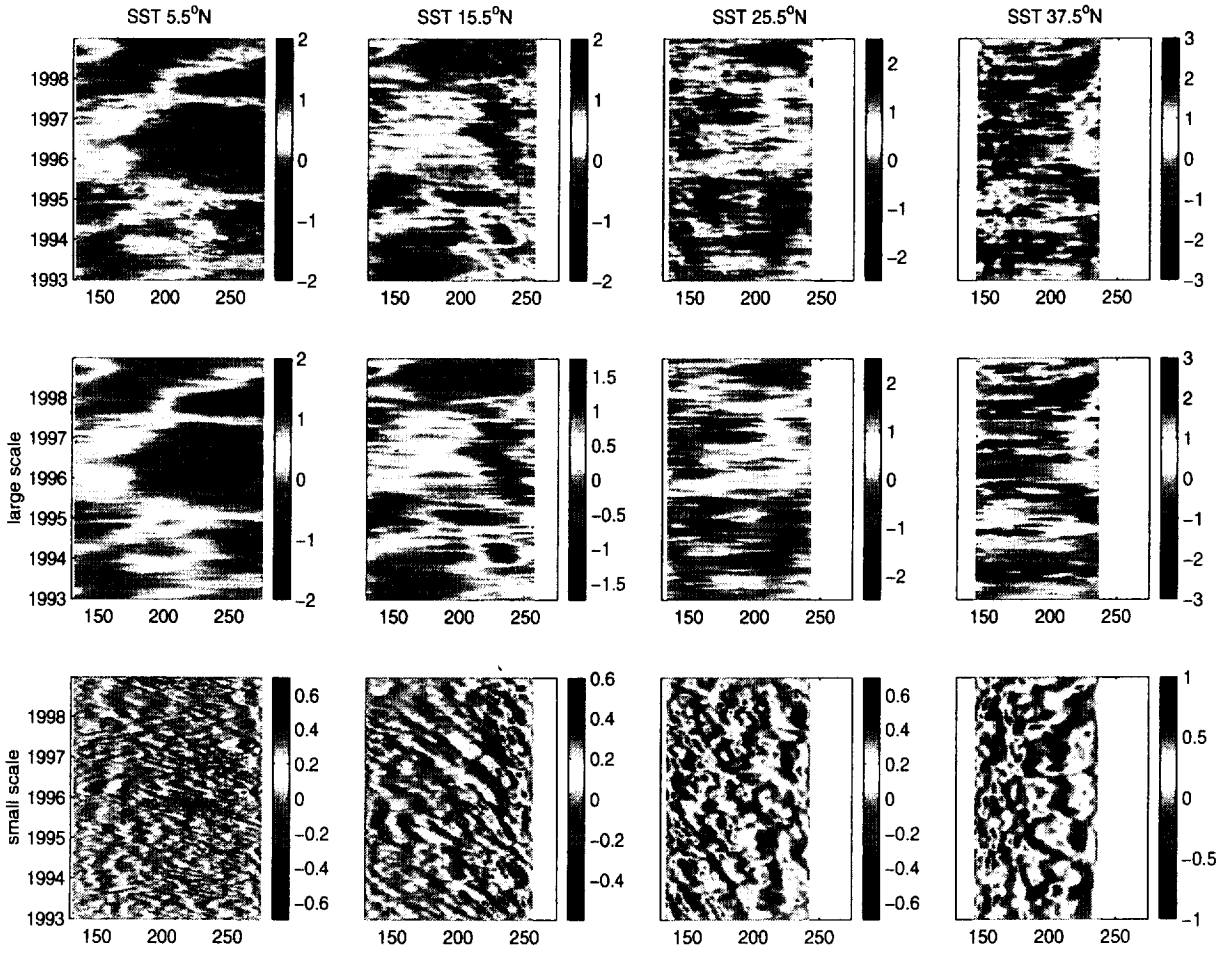
SST 5.5°N
SST 15.5°N
SST 25.5°N
SST 37.5°N
large scale
small scale
1998
1997
1996
1995
1994
1993
150
200
250

Figure 11:

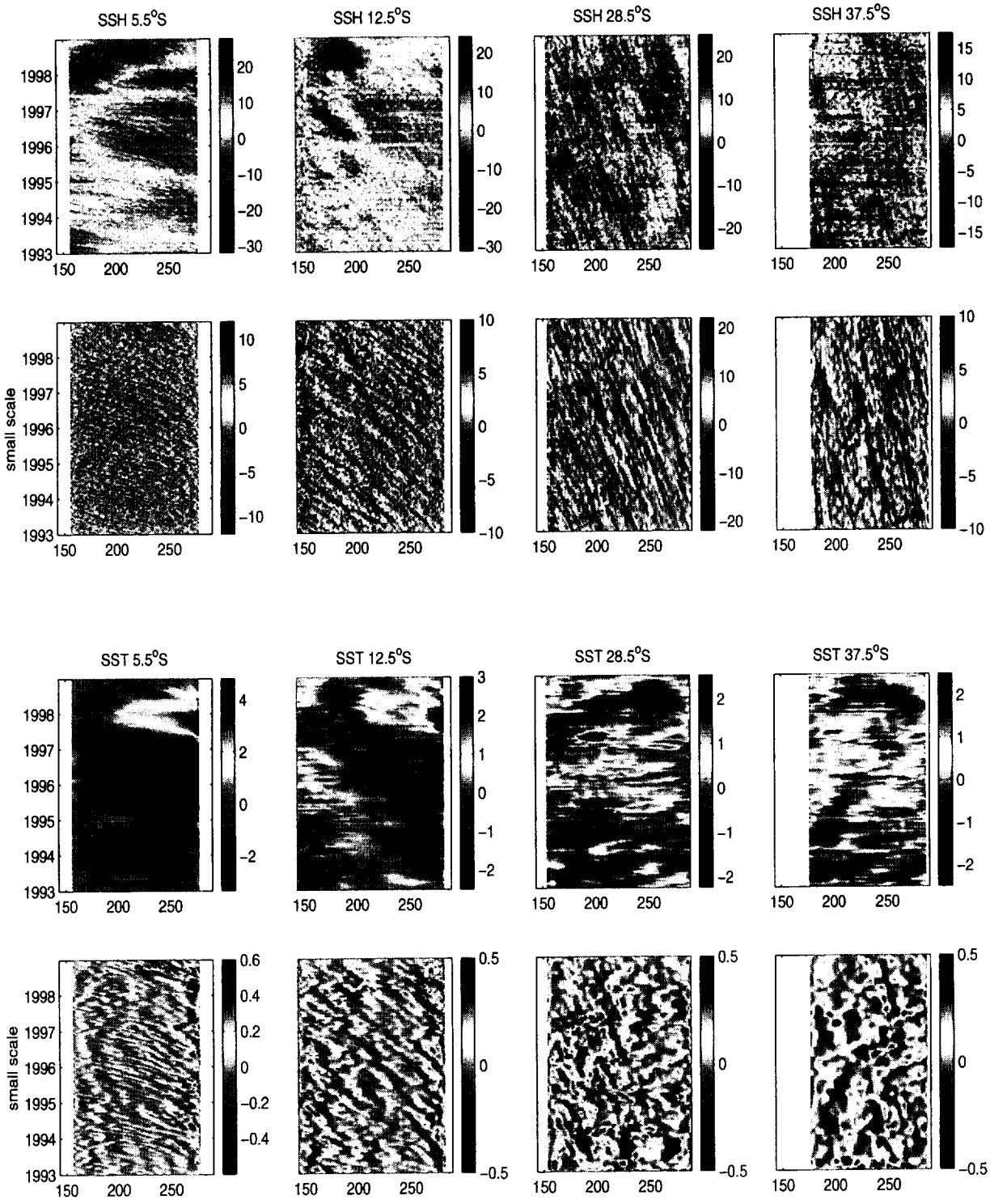
SSH 5.5°S
SSH 12.5°S
SSH 28.5°S
SSH 37.5°S
small scale
SST 5.5°S
SST 12.5°S
SST 28.5°S
SST 37.5°S
small scale
1998
1997
1996
1995
1994
1993
150
200
250

Figure 12:

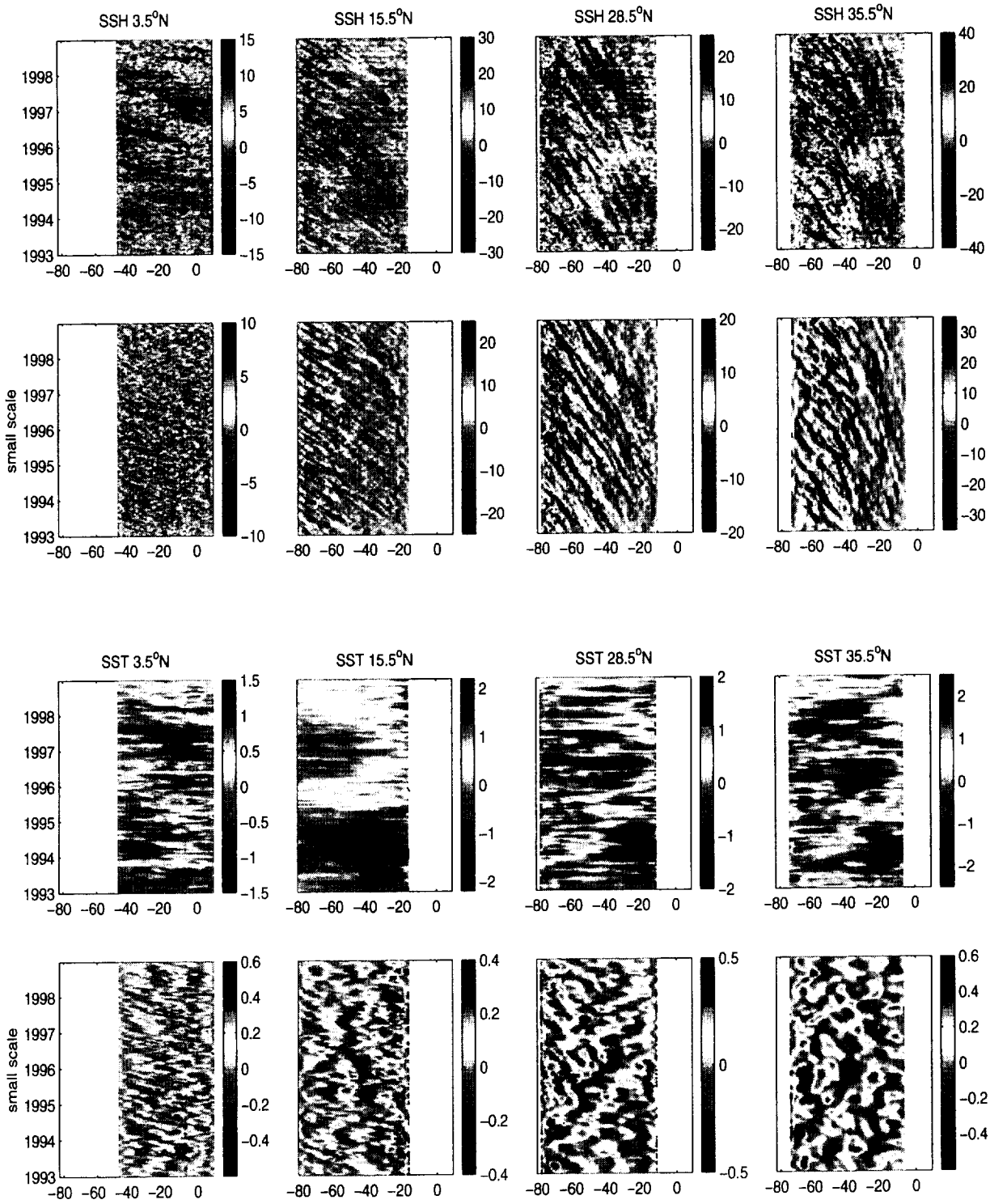
SSH 3.5°N
SSH 15.5°N
SSH 28.5°N
SSH 35.5°N
small scale
SST 3.5°N
SST 15.5°N
SST 28.5°N
SST 35.5°N
small scale

Figure 13:

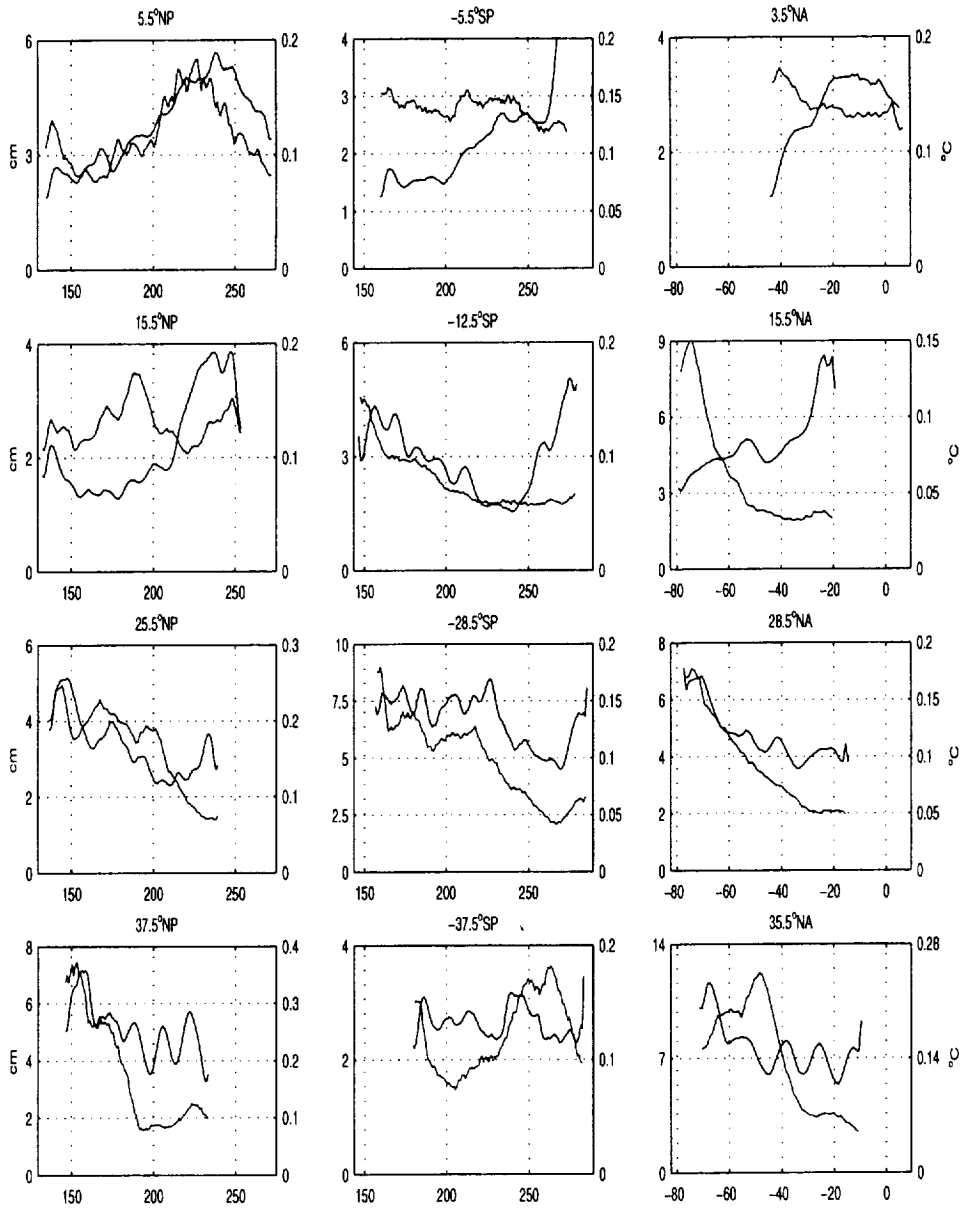
5.5°NP
-5.5°SP
3.5°NA
15.5°NP
-12.5°SP
15.5°NA
25.5°NP
-28.5°SP
28.5°NA
37.5°NP
-37.5°SP
35.5°NA
cm
°C

Figure 14:

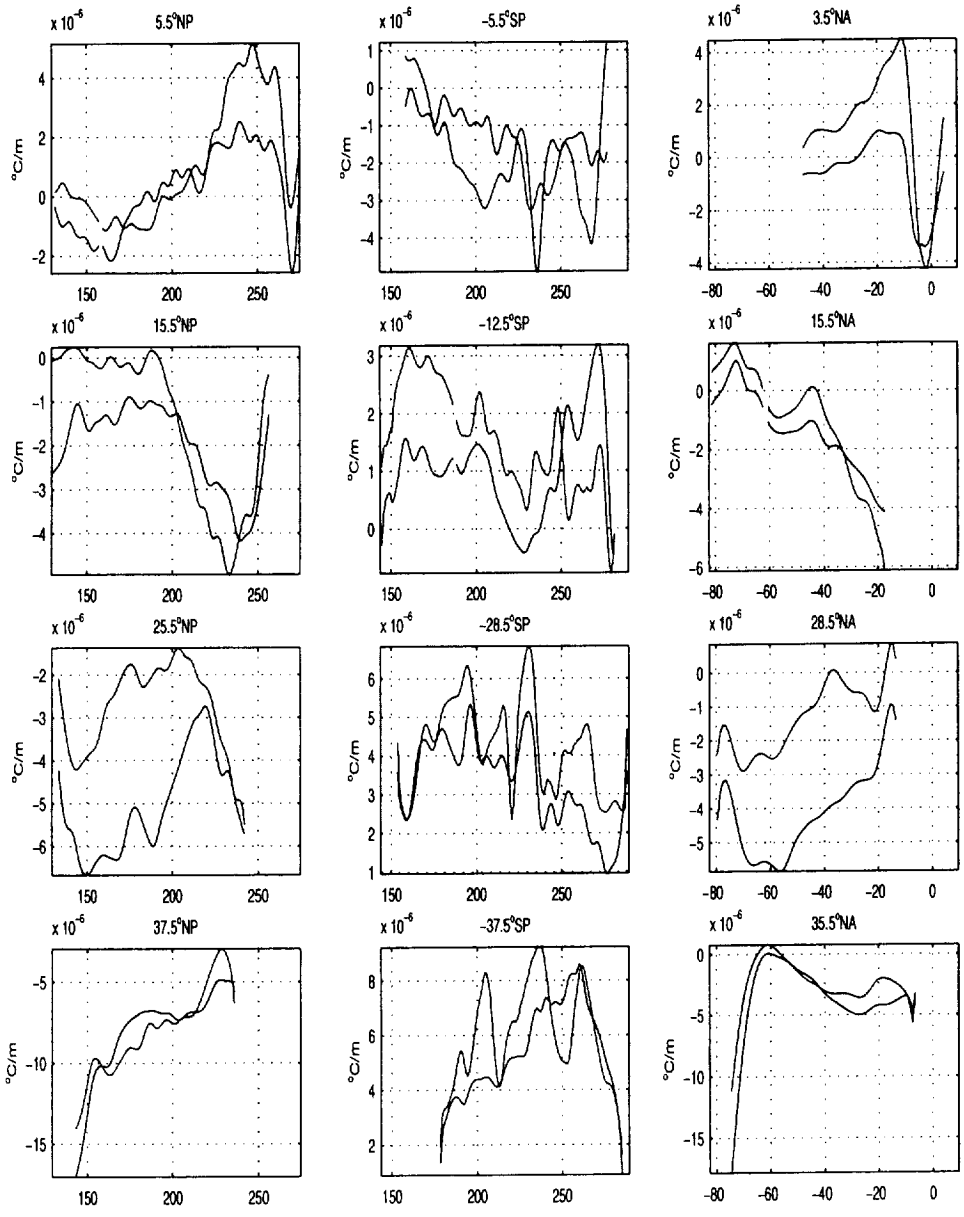
x 10^-6
5.5°NP
-5.5°SP
3.5°NA
15.5°NP
-12.5°SP
15.5°NA
25.5°NP
-28.5°SP
28.5°NA
37.5°NP
-37.5°SP
35.5°NA
°C/m

Figure 15:

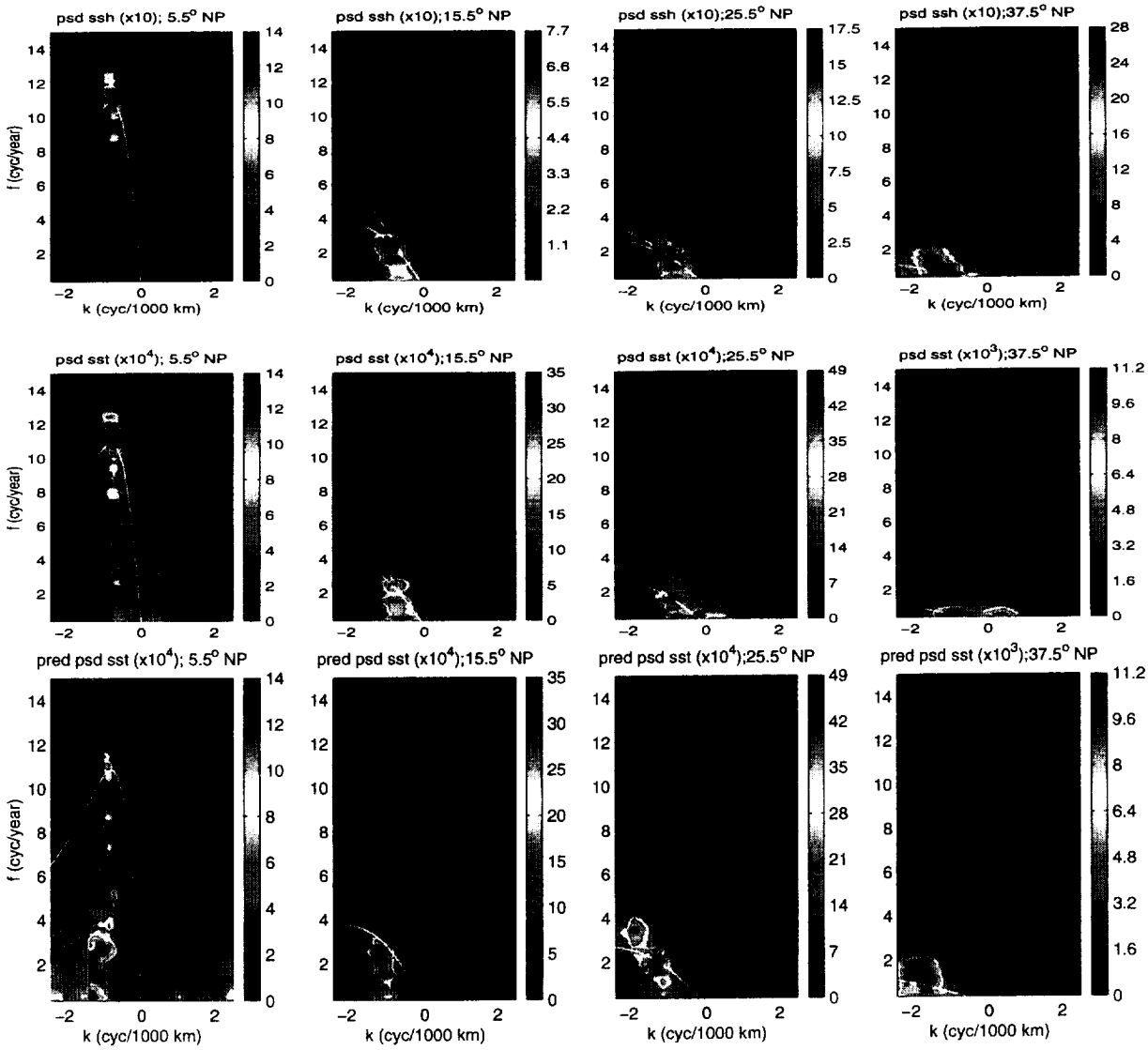
psd ssh (x10); 5.5° NP
psd ssh (x10);15.5° NP
psd ssh (x10);25.5° NP
psd ssh (x10);37.5° NP
psd sst (x10^4); 5.5° NP
psd sst (x10^4);15.5° NP
psd sst (x10^4);25.5° NP
psd sst (x10^3);37.5° NP
pred psd sst (x10^4); 5.5° NP
pred psd sst (x10^4);15.5° NP
pred psd sst (x10^4);25.5° NP
pred psd sst (x10^3);37.5° NP
f (cyc/year)
k (cyc/1000 km)

Figure 16:

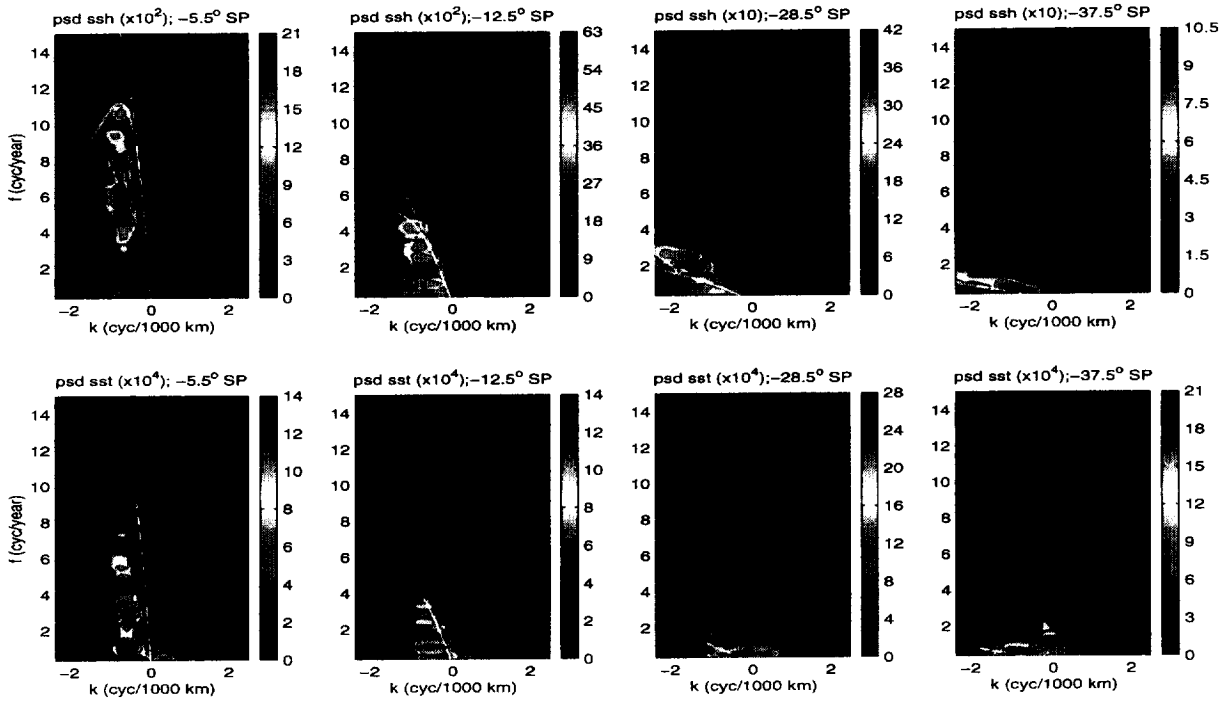
psd ssh (x10^2); −5.5° SP
psd ssh (x10^2);−12.5° SP
psd ssh (x10);−28.5° SP
psd ssh (x10);−37.5° SP
psd sst (x10^4); −5.5° SP
psd sst (x10^4);−12.5° SP
psd sst (x10^4);−28.5° SP
psd sst (x10^4);−37.5° SP
f (cyc/year)
k (cyc/1000 km)

Figure 17:

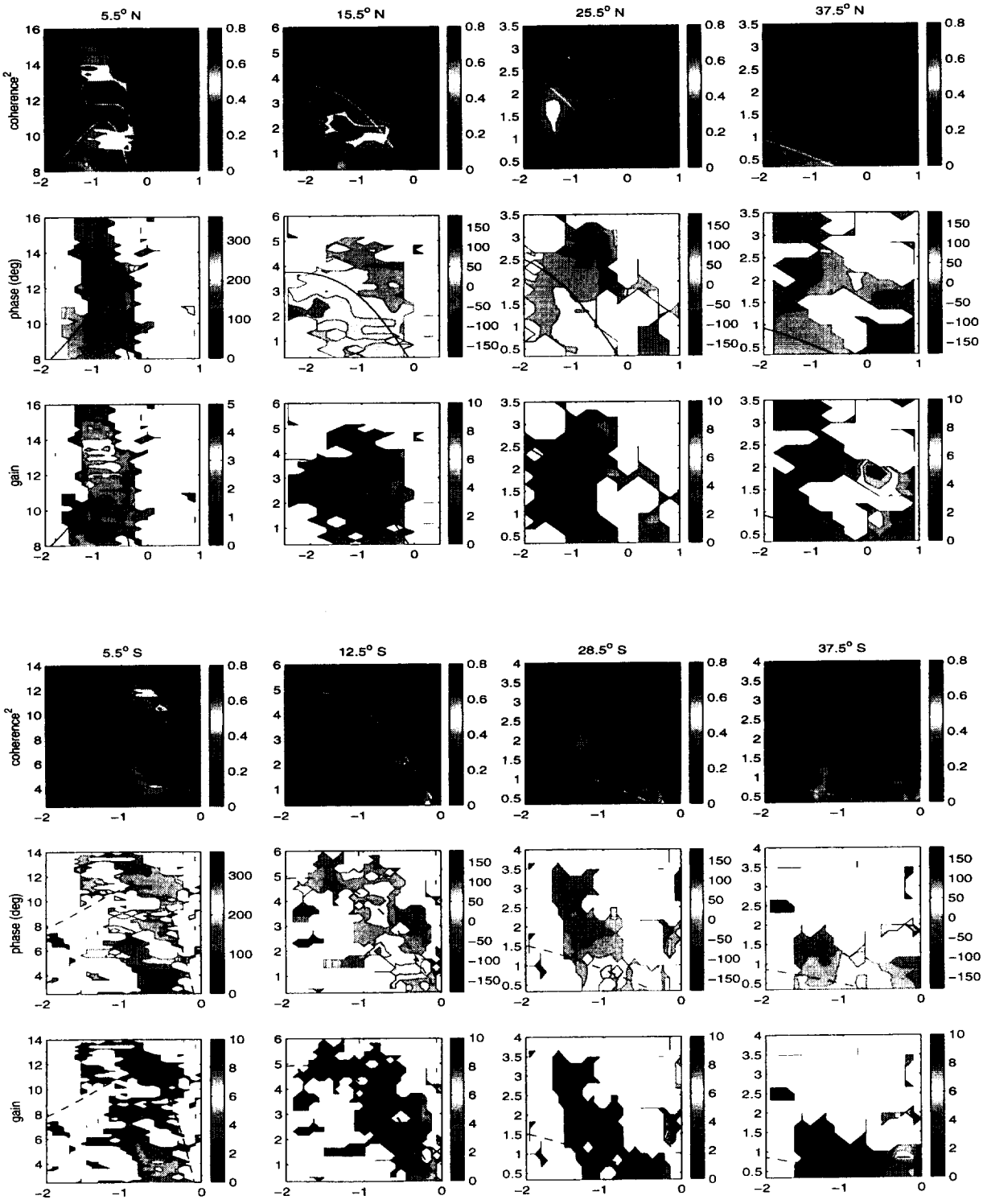
5.5° N
15.5° N
25.5° N
37.5° N
coherence²
phase (deg)
gain
5.5° S
12.5° S
28.5° S
37.5° S

Figure 18:

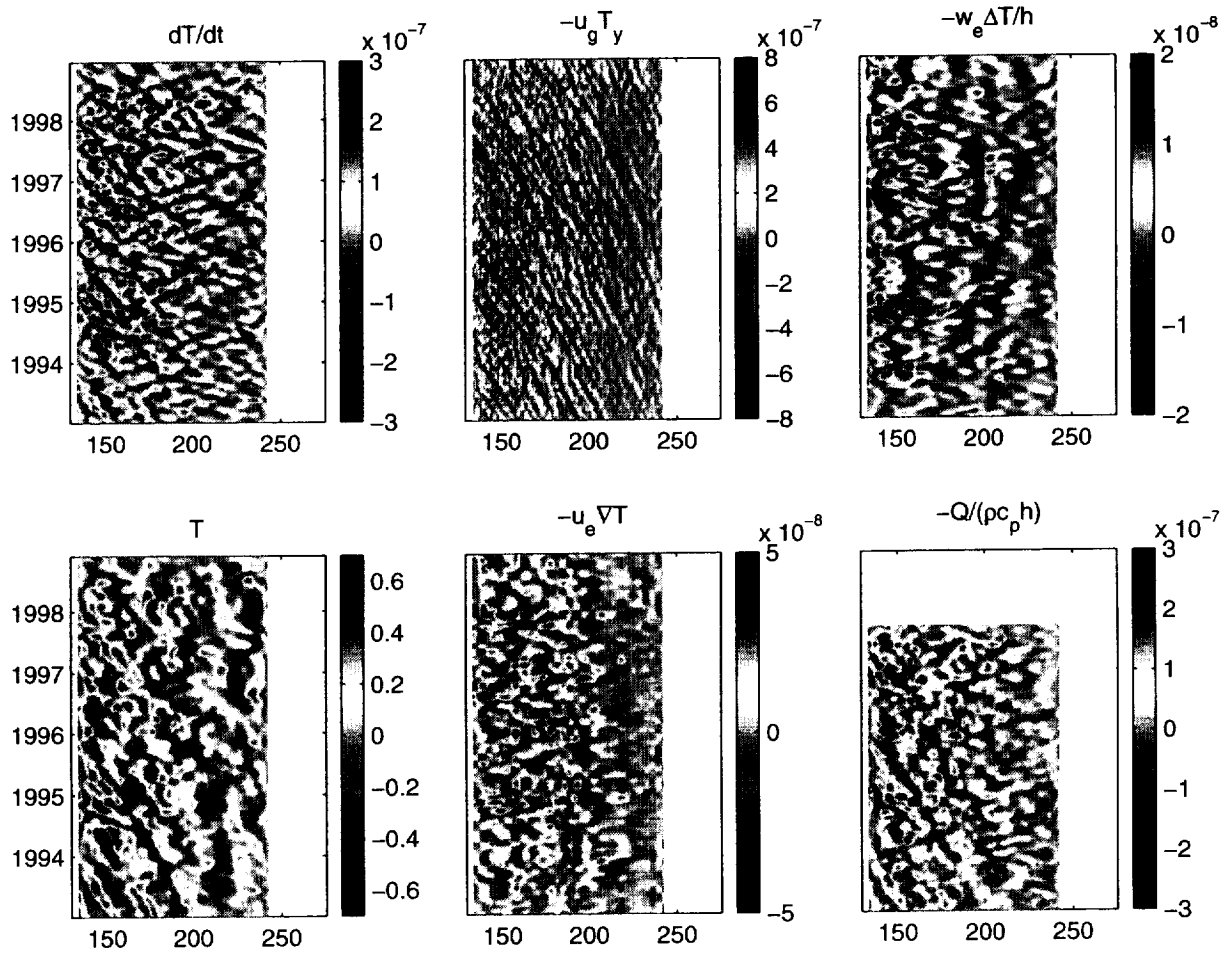
dT/dt
x 10^-7
3
2
1
0
−1
−2
−3
−u_g T_y
x 10^-7
8
6
4
2
0
−2
−4
−6
−8
−w_e ΔT/h
x 10^-8
2
1
0
−1
−2
T
0.6
0.4
0.2
0
−0.2
−0.4
−0.6
−u_e ∇T
x 10^-8
5
0
−5
−Q/(ρc_p h)
x 10^-7
3
2
1
0
−1
−2
−3
1998
1997
1996
1995
1994
150
200
250

Figure 19: